WILEY-VCH

DOI: 10.1002/((please add manuscript number))
Article type: Communication

Ultrathin Transition Metal Dichalcogenide/*3d* Metal Hydroxide Hybridized Nanosheets to Enhance Hydrogen Evolution Activity

Zhengju Zhu, Huajie Yin, Chun-Ting He, Mohammad Al-Mamun, Porun Liu, Lixue Jiang, Yong Zhao, Yun Wang, Hua Gui Yang, Zhiyong Tang, Dan Wang, Xiao-Ming Chen and Huijun Zhao**

Z. Zhu, Dr. H. Yin, Dr. C.-T. He, Dr. M. Al-Mamun, Dr. P. Liu, L. Jiang, Dr. Y. Wang, Prof. Dr. H.-G. Yang, Prof. Dr. Z. Tang, Prof. Dr. D. Wang, Prof. Dr. H. Zhao
Centre for Clean Environment and Energy, Griffith University, Queensland, 4222, Australia
E-mail: h.zhao@griffith.edu.au; h.yin@griffith.edu.au
Prof. Dr. H. Zhao
Centre for Environmental and Energy Nanomaterials, CAS Centre for Excellence in Nanoscience, Institute of Solid State Physics, Chinese Academy of Sciences, Hefei 230031, China
Dr. C.-T. He, Prof. Dr. X.-M. Chen
MOE Key Laboratory of Bioinorganic and Synthetic Chemistry, School of Chemistry, Sun Yat-Sen University, Guangzhou 510275, China
Y. Zhao
ARC Centre of Excellence for Electromaterials Science
Intelligent Polymer Research Institute
AIIM Innovation Campus, University of Wollongong, North Wollongong, NSW 2522, Australia

Keywords: Electrocatalysis, 2D materials, Hydrogen Evolution Reaction, Transition Metal Dichalcogenide, Metal Hydroxide

Abstract: The vast majority of the reported hydrogen evolution reaction (HER) electrocatalysts perform poorly under alkaline conditions due to the sluggish water dissociation kinetics. Herein, we present a hybridization catalyst construction concept to dramatically enhance the alkaline HER activities of 2D-TMDs (MoS_2 and WS_2) based catalysts. A series of ultrathin 2D-hybrids were synthesized *via* facile controllable growth of *3d* metal (Ni, Co, Fe, Mn) hydroxides on the monolayer 2D-TMDs nanosheets. The resultant $Ni(OH)_2$ and $Co(OH)_2$ hybridized ultrathin MoS_2 and WS_2 nanosheets catalysts exhibit significantly enhanced alkaline HER activity and stability compared to their bare counterparts. The 2D-MoS_2/$Co(OH)_2$ hybrid achieved an extremely low overpotential of *ca.*128 mV at 10

mA cm^{-2} in 1 M KOH. The combined theoretical and experimental studies confirm that the formation of the hetero-structured boundaries by suitable hybridization of TMD and *3d* metal hydroxides are responsible for the improved alkaline HER activities because of the enhanced water dissociation step and lower the corresponding kinetic energy barrier by the hybridized *3d* metal hydroxides.

Alkaline hydrogen evolution reaction (HER) plays a critical role in many hydrogen related energy technologies, such as alkaline water electrolysis.[1] To realize an energy-efficient HER, high-performance electrocatalysts are required to promote water reduction process with minimal overpotential and high stability.[1i] However, the vast majority of the reported HER electrocatalysts perform poorly in alkaline electrolytes due to the sluggish water dissociation kinetics.[1b, 2] It is generally accepted that a HER process involves water dissociation (Volmer step, $H_2O + e^- \rightarrow H_{ad} + OH^-$) and H_2 formation (Heyrovsky step, $H_2O + H_{ad} + e^- \rightarrow H_2 + OH^-$, or Tafel step, $2H_{ad} \rightarrow H_2$).[1d, g] One key difference between HER in acidic and alkaline media is that in an alkaline electrolyte, the kinetics are often limited by the sluggish water dissociation step.[1g] Recently, Markovic *et al.* reported a bifunctional strategy to enhance the alkaline HER activity of Pt-based electrocatalysts by electrochemical deposition of *3d* metal hydroxide on Pt surfaces, where the metal hydroxide provides unique active catalyst sites to enhance Volmer step.[1b, f, 2b, 3] We and others have purposely designed a number of Pt-metal hydroxide hybridized electrocatalysts to demonstrate their effectiveness in enhancing alkaline HER activities.[4] However, such a hybridization catalyst design principle has barely been applied to nonprecious earth abundant materials based electrocatalysts. Among nonprecious material candidates for synthesizing hybridized electrocatalysts, the two-dimensional (2D) transition metal dichalcogenide (TMDs) such as MoS_2 and WS_2 nanosheets possess obvious advantages including their demonstrated acidic HER activity, abundance in nature and low cost.[5, 6] More importantly, the exfoliation of TMDs to monolayer structures can boost their HER performance due to the increase in the number and activity of the active sites.[7] Based on the molecular level understanding of HER reaction pathways, it is envisaged that the hybridization catalyst design principle could be applied to construct nonprecious materials based high performance alkaline HER electrocatalysts using monolayer TMD nanosheets and *3d* metal hydroxides as the building blocks.[4a, e]

In this work, we report a series of ultrathin 2D hybridized electrocatalysts synthesized via controllable growth of different *3d* metal hydroxides on monolayer 2D-TMD nanosheets (denoted as 2D-MS_2/M*$(OH)_x$); M = Mo, W; M* = Ni, Co, Fe, Mn). Their alkaline HER activities were found to be governed by the coverage density and properties of M*$(OH)_x$, and the ultrathin feature of 2D-TMDs. These hybrids demonstrated a clear enhancement trend in alkaline HER activities (Mn < Fe << Ni < Co) when compared to their unhybrided counterparts. Impressively, 2D-MoS_2/$Co(OH)_2$ hybridized heterostructures show an extremely low overpotential of 128 mV at 10 mA cm^{-2} in 1 M KOH, which is among the best performed non-Pt alkaline HER electrocatalysts. Density functional theory (DFT) calculations revealed that the introduction of M*$(OH)_x$ onto 2D-TMD surface could effectively reduce the kinetic energy barrier of the water dissociation step to dramatically enhance the alkaline HER catalytic activities.

The synthetic procedure of 2D-MS_2/M*$(OH)_x$ hybrids is schematically depicted in **Figure 1a** (see Supporting Information for details). The facile synthetic procedure can be illustrated using 2D-MoS_2/$Ni(OH)_2$ as a representative example: It can be synthesized by simply treating the well-dispersed monolayer MoS_2 nanosheets (1.0 nm in thickness, Figure S1) obtained from exfoliation of the bulk MoS_2 by Li^+ intercalation[8, 9] with nickel nitrate ($Ni(NO_3)_2 \cdot 6H_2O$) and hexamethylenetetramine (HMT) under hydrothermal conditions. The synthesized hybrids are denoted as 2D-MoS_2/$Ni(OH)_2$-n, n = 5, 10, 20, 40 and 60, corresponding to the added $Ni(NO_3)_2 \cdot 6H_2O$ amount of 5, 10, 20, 40 or 60 mg during synthesis. Figures 1b and 1c show the typical scanning electron microscopy (SEM) and transmission electron microscopy (TEM) images of the as-synthesized 2D-MoS_2/$Ni(OH)_2$-10 nanosheets. It is evident that the hybrid nanosheets maintained its 2D ultrathin feature, and the nickel hydroxide species were uniformly formed on the surface of MoS_2 without agglomeration. The homogeneity of the grown $Ni(OH)_2$ on 2D-MoS_2 nanosheets was subsequently recognized by the corresponding TEM elemental mapping (Figure 1d), in which the observed Ni, O, Mo and

S elements are evenly distributed. As revealed by the high-resolution TEM (HRTEM) image (Figures 1e), $Ni(OH)_2$ nanoparticles (NPs) with well-defined β-$Ni(OH)_2$ phase lattice space are formed on the MoS_2 nanosheets. The dash cycles indicate the boundaries between $Ni(OH)_2$ NPs and 2D-MoS_2 nanosheet substrate. The atomic-resolution high angle annular dark field scanning transmission electron microscope (HAADF-STEM) images of 2D-MoS_2/$Ni(OH)_2$-10 (Figures 1f and S3) further reveal clear boundaries between the coated $Ni(OH)_2$ NPs and 2D-MoS_2 nanosheet substrate. The atomic force microscopy (AFM) image (Figure 1g) shows well-preserved 2D ultrathin feature of 2D-MoS_2/$Ni(OH)_2$-10 nanosheets with a thickness of ~5 nm, approximately 5 time thicker than that of the monolayer MoS_2 nanosheets substrate (~1 nm, Figure S1 in Supporting Information). The crystalline characteristics of $Ni(OH)_2$ NPs are also corroborated by X-ray diffraction (XRD, Figure S4a), in which a part of diffraction peaks can be respectively indexed to (001), (100), (101) and (110) reflections of β-phase $Ni(OH)_2$ (JCPDS No. 14-0117). A slightly reduced d-spacing of (002) plane of MoS_2 in the hybrid was observed, which could be due to that the in-situ grown metal hydroxide nanoparticle layer can slightly compress the (002) plane of stacked 2D-MoS_2 nanosheets. This can be further confirmed by the line profiling of HRTEM image (Figure S4b). The XRD analysis also excludes the formation of Ni-Mo-S compounds.[10] The determined $Ni(OH)_2$ contents in 2D-MoS_2/$Ni(OH)_2$-10 by the inductively coupled plasma mass spectrometry (ICP-MS) analysis and TGA measurements (Figure S5) are found to be 15.6 wt.% and 13.6 wt.%, respectively.

X-ray absorption spectroscopy (XPS) measurements were carried out to investigate the compositional and chemical states of 2D-MoS_2/$Ni(OH)_2$-10 hybrid. For the bulk MoS_2, the Mo 3d spectrum consists of peaks at 229.3 and 232.5 eV, corresponding to Mo^{4+} $3d_{5/2}$ and Mo^{4+} $3d_{3/2}$ components of 2H phase MoS_2 (Figure 2a).[9] In its S 2p spectrum (Figure 2b), the known doublet peaks of 2H phase MoS_2, S $2p_{1/2}$ and S $2p_{3/2}$ are located at 163.3 and 162.1 eV, respectively. The additional peaks (green lines) observed from the monolayer MoS_2

nanosheets and 2D-MoS_2/$Ni(OH)_2$-10 confirm the occurrence of a partial transformation of 2H to 1T phase in the exfoliated 2D-MoS_2, which can be stably retained in the hybrids after growing $Ni(OH)_2$.[7a, b, 9] The HAADF-STEM, Raman and UV-Vis spectra of 2D-MoS_2/$Ni(OH)_2$-10 further confirm that the conductive 1T phase of 2D-MoS_2 can still be preserved (Figure S3, S6 and S7).[7a, b] It can be discerned by Ni 2p XPS spectra (Figure 2c) that Ni species is in their Ni (II) state.[4a, 11] The measured 0.2 eV difference of the main Ni^{2+} peaks from 2D-MoS_2/$Ni(OH)_2$-10 and $Ni(OH)_2$ indicates that a noticeable charge transfer between $Ni(OH)_2$ and 2D-MoS_2 is unlikely. The presence of OH^- groups and Ni-O bonds further indicate the existence of $Ni(OH)_2$ in the as-synthesized hybrids (Figure 2d).[12] The Fourier transform infrared spectroscopy (FTIR) was performed to further confirm XPS results. The main characteristic bands associated with MoS_2 and $Ni(OH)_2$ are clearly visible (Figure 2e), confirming the successful growth of $Ni(OH)_2$ onto the MoS_2 nanosheets. In detail, the small sharp peak at 3643 cm^{-1} can be assigned to the stretching vibrational mode of non-hydrogen-bonded hydroxyl groups in the brucite-like sheets inherited from $Ni(OH)_2$,[13] while a clear band centred at 467 cm^{-1} is due to the contributions of stretching vibration actions of Ni-OH and Mo-S from $Ni(OH)_2$ and MoS_2, respectively.[9] Figure 2f shows the typical cyclic voltammetric (CV) curves (0-0.6 V *vs.* RHE) of 2D-MoS_2/$Ni(OH)_2$-10. The observed $Ni^{2+}\rightarrow Ni^{3+/4+}$ redox peaks (ca. 0.35-0.5 V vs RHE) further confirm the presence of nickel hydroxide species.[12] In a brief summary, the above evidences demonstrate the successful growth of $Ni(OH)_2$ NPs onto ultrathin 2D-MoS_2 nanosheets substrate. Beyond 2D-MoS_2/$Ni(OH)_2$-10, a series of ultrathin 2D-nanosheets hybrids made of other *3d* metal hydroxides ($M^*(OH)_x$, M*=Co, Fe, Mn) on the monolayer MoS_2 and WS_2 nanosheets were also successfully synthesized. Their morphologies and structures were identified using SEM, TEM, XRD, XPS, FTIR and electrochemical techniques as shown in Figures S8 to S15.

The alkaline HER performance of 2D-MoS_2/$Ni(OH)_2$-10 and other comparison electrocatalysts were evaluated using a three-electrode electrochemical cell with a rotating disc working electrode in N_2-saturated 0.1 and 1 M KOH electrolyte solutions. The HER polarization curves (with *iR* correction) of 2D-MoS_2/$Ni(OH)_2$-10 along with the bare 2D-MoS_2, $Ni(OH)_2$ and the benchmark commercial Pt/C (20 wt.% Pt) are presented in Figures 3 and S16. Noticeably, the growth of $Ni(OH)_2$ NPs on the monolayer MoS_2 nanosheets leads to a profoundly enhanced alkaline HER activity. Seen from Figure S16, the HER overpotential (at 10 mA cm^{-2}) of 2D-MoS_2/$Ni(OH)_2$-10 in 0.1 M KOH dramatically decreased to 240 mV from 640 mV of the bare 2D-MoS_2, while under the same experimental conditions, $Ni(OH)_2$ is almost inactive for HER. The HER activity under strong alkaline condition (1 M KOH) was also investigated (Figure 3a). The overpotential of 2D-MoS_2/$Ni(OH)_2$-10 at 10 mA cm^{-2} is 185 mV, substantially lower than that of the bare MoS_2 (351 mV) and many reported MoS_2-based electrocatalysts including defeat-rich MoS_2 nanosheets (~190 mV in acidic solution),[14] double-gyroid mesoporous MoS_2 film (~235 mV)[5c] and CoS_x/MoS_2 composites (~220 mV at 5 mA cm^{-2}).[15] As shown in Figure 3b, the Tafel slope of 2D-MoS_2/$Ni(OH)_2$-10 is 73 mV per decade, which is much smaller than that of the bare MoS_2 (156 mV per decade). Such an obviously decreased Tafel slope highlights an effectively accelerated HER kinetics by growing $Ni(OH)_2$ on 2D-MoS_2. To further confirm the vital role of $Ni(OH)_2$ in 2D-MoS_2/$Ni(OH)_2$-10, the $Ni(OH)_2$ in the hybrid was etched by the diluted H_2SO_4 (Figure S17). The Ni content in the etched 2D-MoS_2/$Ni(OH)_2$-10 determined by ICP-MS and SEM-EDS are found to be 2.4 at.% and 2.7 at.%, respectively, suggesting ~85% of Ni have been removed (Figure S17c). Although this etched product still retains the 2D morphology (Figures S17a and b), but exhibits a significantly reduced HER activity that closes to the bare 2D-MoS_2 (Figure S17d). This confirms the critical role of $Ni(OH)_2$ to accelerate HER kinetics.

In order to unveil the contributions of the ultrathin feature to the superior electrocatalytic activity, the HER performance of the bulk MoS_2 and MoS_2/$Ni(OH)_2$ hybrids (Figures 3a and

S18) were conducted. As shown in Figure 3a, the bulk counterparts exhibit inferior HER activities compared to 2D-MoS_2/$Ni(OH)_2$-10. There are two distinctive advantages of 2D-MoS_2 as the substrate to construct high performance HER electrocatalyst: (i) the ultrathin feature of 2D MoS_2 provides high electrochemical surface area and (ii) partially converted conductive 1T phase benefits kinetics and electron transfer.[7] Interestingly, the enhancement effect of the metal hydroxide is still observable from the bulk MoS_2/$Ni(OH)_2$. Additionally, the ratio of MoS_2 to $Ni(OH)_2$ could be an important factor for the HER performance of the hybrids. Figure S19 shows the HER activities of MoS_2/$Ni(OH)_2$-n (n = 5, 10, 20, 40, 60) in 1 M and 0.1 M KOH electrolyte solutions. Clearly, 2D-MoS_2/$Ni(OH)_2$-10 possesses a minimal HER overpotential, indicating that an optimum HER activity can only be obtained from a optimal $Ni(OH)_2$ coverage on MoS_2 nanosheets (Figures S19 and S20).

The stabilities of 2D-MoS_2/$Ni(OH)_2$-10, bare 2D-MoS_2 and commercial Pt/C are shown in Figure 3c. Impressively, 2D-MoS_2/$Ni(OH)_2$-10 can achieve a negligible loss in HER activity with an approximately 1 mV increase in the overpotential at 10 mA cm^{-2} after 1000 cycles. In contrast, the HER overpotentials of the bare MoS_2 and commercial Pt/C were noticeably increased. Therefore, the introduction of $Ni(OH)_2$ enhances not only the HER activity of the ultrathin MoS_2 but also the stability of MoS_2 in strong basic reaction medium, which was also observed in our previous work.[4a] We also performed chronoamperometry (CA) stability test (20 hours under an initial current density of 10 mA cm^{-2}) of 2D-MoS_2 and 2D-MoS_2/$Ni(OH)_2$-10 in 1 M KOH with the applied potentials of -0.35 V and -0.19 V vs RHE, respectively (Figure S21). The 2D-MoS_2 displayed a rapid current density decay under an applied potential of -0.35 V and can only retain 28% of its initial current density after 20 h. While 2D-MoS_2/$Ni(OH)_2$-10 are capable of retaining 94% of its initial current density after 20 h. These results further confirm the superior stability of 2D-MoS_2/$Ni(OH)_2$-10. In addition, Figure S22 shows the SEM images and EDS spectra of 2D-MoS_2/$Ni(OH)_2$-10 after the CA stability test. The corresponding SEM images (Figure S22) reveal a well-maintained ultrathin 2D feature

without structural deformation. The EDS spectra obtained after the CA stability test reveal that the ratio of metal hydroxide to MoS_2 is almost unchanged, indicating an excellent compositional stability of 2D-MoS_2/$Ni(OH)_2$. Recently, Markovic *et al.* suggested that the HER stability and activity are dependent on the structure/properties of the unit building blocks.[15] In their $CoMoS_x$, the less stable CoS_x component could be stabilized by the stable MoS_x component through the hybridization to form $CoMoS_x$.[15] In our 2D-MoS_2/$Ni(OH)_2$, the enhanced stability could be due to the suppressed physical ripening and dissolution of MoS_2 component by the alkaline stable $Ni(OH)_2$ nanostructures.

On the basis of the experimental evidences presented above, it is reasonable to assume that the superior alkaline HER activity of 2D-MoS_2/$Ni(OH)_2$-10 is resulted from the boundaries formed by the edges of the $Ni(OH)_2$ NPs on the surface of the 2D-MoS_2 nanosheets. Such boundaries possess unique interfacial hetero-structures resulting from the rich $Ni(OH)_2$ edge defects hybridized with the surface of 2D-MoS_2 nanosheets. The hybridized $Ni(OH)_2$ and MoS_2 on the opposed sides of the boundary can act synergistically to accelerate H_2O dissociation and H_2 formation steps of HER. The hybridised $Ni(OH)_2$ side of the boundary favourable for H_2O adsorption, accelerating the water dissociation step to enhance the production of H* and OH^- ($H_2O \rightarrow H^* + OH^- + e^-$).[1b, f, 2a] The produced OH^- and H* are rapidly adsorbed respectively by the hybridized $Ni(OH)_2$ (OH_{ad}) and MoS_2 (H_{ad}) on the opposite side of the boundary where H_{ad} is simultaneously combined to produce H_2 via Heyrovsky ($H_2O + H_{ad} + e^- \rightarrow H_2 + OH^-$) and/or Tafel ($2H_{ad} \rightarrow H_2$) processes. When H_2 formation proceeds *via* Heyrovsky process, the produced OH^- could be timely removed by the hybridized $Ni(OH)_2$, which not only accelerates Heyrovsky process but also prevent the active H_2 formation sites on MoS_2 from inhibition by OH_{ad}.

To further confirm the synergistic effect of the hetero-structured boundaries, the alkaline HER performance of other ultrathin 2D hybrids were systemically investigated. It is expected

that the hybridization of different *3d* metal hydroxides would lead to distinct HER activities. The HER polarization curves for 2D-MoS_2 and 2D-WS_2 based hybrids in 0.1 M and 1 M KOH are shown in Figure S23. The alkaline HER activities are expressed as the measured overpotential at 5 mA cm^{-2} current density (Figure 3d). These hybrids show a clear alkaline HER activity trend of different *3d*-metal hydroxides. The alkaline HER activities of the 2D-MoS_2 and 2D-WS_2 based M*$(OH)_x$ hybrids are in an order of Mn < Fe << Ni < Co and Mn < Fe << Co < Ni, respectively. The ECSA-normalized HER polarization curves, exchange current densities and turnover frequencies (TOF) of 2D-MoS_2 based hybrids were obtained (Figure S24, S25 and Table S1). As expected, the exchange current densities of 2D-MoS_2/$Co(OH)_2$ and 2D-MoS_2/$Ni(OH)_2$-10 are 0.239 and 0.178 mA cm^{-2}, much higher than that of the bare 2D-MoS_2 (0.067 mA cm^{-2}). The TOF values (at overpotential of 200 mV) of 2D-MoS_2/$Co(OH)_2$ and 2D-MoS_2/$Ni(OH)_2$ are 4.31 and 1.61 s^{-1}, which are much larger than that of the bare 2D-MoS_2 (0.115 s^{-1}). These results show a clear alkaline HER activity enhancement trend by hybridization of 2D-MoS_2 with $Co(OH)_2$ and $Ni(OH)_2$ species. Impressively, 2D-MoS_2/$Co(OH)_2$ with optimized ratio of $Co(OH)_2$ to MoS_2 shows an extremely low onset potential of 70 mV, an overpotential of 128 mV at 10 mA cm^{-2} and excellent stability in 1 M KOH (Figures 3a and S26). Such a superior HER performance surpasses the most TMD-based HER electrocatalysts reported so far and is among the best nonprecious metal based electrocatalysts in alkaline media (Table S2). Both 2D-MoS_2 and 2D-WS_2 hybridized with $Co(OH)_2$ display significantly enhanced HER activities similar to those with $Ni(OH)_2$. This implies that Ni and Co hydroxides possess a balanced strength between the adsorption of H_2O and desorption of OH_{ad}. However, 2D-MoS_2 and 2D-WS_2 hybridized with $Mn(OH)_2$ and $Fe(OH)_3$ show inferior HER activities, especially for $Mn(OH)_2$. This could be caused by too strong adsorption strength of these metal hydroxides towards OH_{ad} that makes OH_{ad} desorption very difficult, leading to an accumulated OH_{ad} on the catalytic active sites that inhibit H_2O dissociation.[2b]

DFT calculations on the reaction pathway of H_2O dissociation step (ΔG_W, Volmer step) and the chemisorption energies of hydroxide (ΔE_{OH}) of MoS_2 and MoS_2-based hybrids were performed to gain further insight on the synergistic effect of the hetero-structured boundaries. As shown in Figure 4a, the free energy change of the Volmer reaction (ΔG_R) for MoS_2 (1.16 eV) is lower than that for $MoS_2/Ni(OH)_2$ (1.60 eV), indicating the $MoS_2/Ni(OH)_2$ composite is thermodynamic unfavourable for H_2O dissociation. However, with the assistance of $Ni(OH)_2$, the water dissociation kinetic energy barrier (ΔG_W) can be drastically decreased from 2.48 to 1.83 eV, revealing a kinetically-controlled process. Importantly, the kinetics of the water dissociation step can be effectively promoted by the hybridization of MoS_2 with $Ni(OH)_2$. The situations are similar for the cases of $MoS_2/Co(OH)_2$ and $MoS_2/Fe(OH)_3$ where ΔG_W can be reduced by 1.30 and 0.58 eV, respectively, but the later possesses much lower ΔE_{OH} (-3.85 eV) than that of the former (-2.75 eV) as well as the bare MoS_2 (-1.35 eV), which could lead to difficulties in desorption that can inhibit the active sites for re-adsorption of water molecule (Figure 4b). Particularly, $MoS_2/Mn(OH)_2$ hybrid exhibits both high ΔG_W (-3.69 eV) and ΔE_{OH} (-3.70 eV), resulting in the worst HER performance. Generally, govern by the low chemisorption energies, OH^- take a prone position to adsorb on the *3d* metal hydroxides/TMD hybrids, which, on one hand, facilitates H_2O dissociation to some extents, on the other hand, blocks the consequent reactions. Thus, the moderate ΔE_{OH} values of $MoS_2/Ni(OH)_2$ (-2.47 eV) and $MoS_2/Co(OH)_2$ (-2.75 eV) hold a favourable balance between facilitating water dissociation and preventing the water dissociation active sites from inhibition by the strongly adsorbed hydroxides. In a word, the DFT calculation results are well consistent with the experimental observations and confirm that the hetero-structured boundaries created through the hybridization of TMD with 3*d*-metal hydroxide is effective to enhance alkaline HER performance.

In summary, we have demonstrated a hybridization concept capable of dramatically enhancing the alkaline HER activities of 2D-TMDs based catalysts. A facile method was

presented to synthesize ultrathin 2D hybrids by controllable growth of *3d* metal (Ni, Co, Fe, Mn) hydroxides on monolayer 2D MoS_2 and WS_2 nanosheets. Among the investigated hybrids, 2D-MoS_2/$Ni(OH)_2$ and 2D-MoS_2/$Co(OH)_2$ display excellent alkaline HER catalytic performances. The combined theoretical and experimental studies demonstrate that the formation of hetero-structured boundaries *via* appropriate hybridization of TMD and *3d* metal hydroxides can effectively promote the crucial water dissociation step kinetics by lowering the kinetic energy barrier to enhance alkaline HER performance. The findings of this work provide a new means to enable the development of high performance alkaline HER electrocatalysts using cheap and plentiful transition metal-based materials.

Supporting Information
Supporting Information is available from the Wiley Online Library or from the author.

Acknowledgements
Z. Z., H. Y., and C.-T. H. contributed equally to this work. This work was financially supported by the Australian Research Council (ARC) Discovery Project (DP170104834), the National Natural Science Foundation of China (51372248 and 51432009) and Griffith University Postdoctoral Fellowship. Chun-Ting He is thankful to the National Postdoctoral Program for Innovative Talents (BX201600195). The authors gratefully acknowledge Dr. Gilberto Casillas from University of Wollongong for his help with the HAADF-STEM charaterizaiton.

Received: ((will be filled in by the editorial staff))
Revised: ((will be filled in by the editorial staff))
Published online: ((will be filled in by the editorial staff))

References

[1] a) K. Zeng, D. Zhang, *Prog. Energy Comb. Sci.* **2010**, *36*, 307-326; b) R. Subbaraman, D. Tripkovic, D. Strmcnik, K. C. Chang, M. Uchimura, A. P. Paulikas, V. Stamenkovic, N. M. Markovic, *Science* **2011**, *334*, 1256-1260; c) Y. Zheng, Y. Jiao, M. Jaroniec, S. Z. Qiao, *Angew. Chem.* **2015**, *54*, 52-65; d) Y. Jiao, Y. Zheng, M. Jaroniec, S. Z. Qiao, *Chem. Soc. Rev.* **2015**, *44*, 2060-2086; e) V. R. Stamenkovic, D. Strmcnik, P. P. Lopes, N. M. Markovic, *Nat. Mater.* **2017**, *16*, 57-69; f) J. H. Montoya, L. C. Seitz, P. Chakthranont, A. Vojvodic, T. F. Jaramillo, J. K. Norskov, *Nat. Mater.* **2017**, *16*, 70-81; g) Z. W. Seh, J. Kibsgaard, C. F.

Dickens, I. Chorkendorff, J. K. Norskov, T. F. Jaramillo, *Science* **2017**, *355*, eaad4998; h) Y. Zheng, Y. Jiao, S. Qiao, A. Vasileff, *Angew. Chem.* **2017**, DOI: 10.1002/anie.201710556; i) J. Mahmod, F. Li, S.-M. Jung, M. S. Okyay, I. Ahmad, S.-J. Kim, N. Park, H. Y. Jeong, J.-B. Baek, *Nat. Nanotech.* **2017**, *12*, 441-446.

[2] a) N. Danilovic, R. Subbaraman, D. Strmcnik, K. C. Chang, A. P. Paulikas, V. R. Stamenkovic, N. M. Markovic, *Angew. Chem. Int. Ed.* **2012**, *51*, 12495-12498; b) R. Subbaraman, D. Tripkovic, K. C. Chang, D. Strmcnik, A. P. Paulikas, P. Hirunsit, M. Chan, J. Greeley, V. Stamenkovic, N. M. Markovic, *Nat. Mater.* **2012**, *11*, 550-557; c) I. Ledezma-Yanez, W. D. Z. Wallace, P. Sebastián-Pascual, V. Climent, J. M. Feliu, M. T. M. Koper, *Nat. Energy* **2017**, *2*, 17031; d) Z. Zeng, K.-C. Chang, J. Kubal, N. M. Markovic, J. Greeley, *Nat. Energy* **2017**, *2*, 17070.

[3] D. Strmcnik, P. P. Lopes, B. Genorio, V. R. Stamenkovic, N. M. Markovic, *Nano Energy* **2016**, *29*, 29-36.

[4] a) H. Yin, S. Zhao, K. Zhao, A. Muqsit, H. Tang, L. Chang, H. Zhao, Y. Gao, Z. Tang, *Nat. Commun.* **2015**, *6*, 6430; b) L. Wang, C. Lin, J. Chen, D. Huang, L. Jiang, M. Wang, L. Chi, L. Shi, J. Jin, *ACS Catal.* **2015**, *5*, 3801-3806; c) L. Wang, Y. Zhu, Z. Zeng, C. Lin, M. Giroux, L. Jiang, Y. Han, J. Greeley, C. Wang, J. Jin, *Nano Energy* **2017**, *31*, 456-461; d) P. Wang, K. Jiang, G. Wang, J. Yao, X. Huang, *Angew. Chem.* **2016**, *128*, 13051-13055; e) H. Yin, Z. Tang, *Chem. Soc. Rev.* **2016**, *45*, 4873-4891.

[5] a) B. Hinnemann, P. G. Moses, J. Bonde, K. P. Jørgensen, J. H. Nielsen, S. Horch, I. Chorkendorff, J. K. Nørskov, *J. Am. Chem. Soc.* **2005**, *127*, 5308-5309; b) T. F. Jaramillo, K. P. Jørgensen, J. Bonde, J. H. Nielsen, S. Horch, I. Chorkendorff, *Science* **2007**, *317*, 100-102; c) J. Kibsgaard, Z. Chen, B. N. Reinecke, T. F. Jaramillo, *Nat. Mater.* **2012**, *11*, 963-969; d) H. Li, C. Tsai, A. L. Koh, L. Cai, A. W. Contryman, A. H. Fragapane, J. Zhao, H. S. Han, H. C. Manoharan, F. Abild-Pedersen, J. K. Norskov, X. Zheng, *Nat. Mater.* **2015**; e) M. Chhowalla, H. S. Shin, G. Eda, L. J. Li, K. P. Loh, H. Zhang, *Nat. Chem.* **2013**, *5*, 263-275; f) C. Tan, H.

Zhang, *Nat. Comm.* **2015**, *6*, 7873; g) Q. Lu, Y. Yu, Q. Ma, B. Chen, H. Zhang, *Adv. Mater.* **2016**, *28*, 1917-1933.

[6] a) H. Wang, C. Tsai, D. Kong, K. Chen, F. Abild-Pedersen, J. K. Norskov, Y. Cui, *Nano Res.* **2015**, *8*, 566-575; b) J. Deng, H. Li, J. Xiao, Y. Tu, D. Deng, H. Yang, H. Tian, J. Li, P. Ren, X. Bao, *Energy Environ. Sci.*, **2015***, 8*, 1594-1601; c) J. Zhang, T. Wang, P. Liu, S. Liu, R. Dong, X. Zhuang, M. Chen, X. Feng, *Energy Environ. Sci.*, **2016**, *9*, 2789-2793; d) X.-Y. Yu, Y. Feng, Y. Jeon, B. Guan, X. W. Lou, U. Paik, *Adv. Mater.* **2016**, *28*, 9006-9011; e) B. Zhang, J. Wang, Y. Ruan, X. Ji, K. Xu, C. Chen, H. Wan, L. Miao, J. Jiang, *Nano Energy,* **2017**, *37*, 74-80; f) X. Zhang, Y. Liang, *Adv. Sci.* **2018**, 5, 1700644.

[7] a) M. A. Lukowski, A. S. Daniel, F. Meng, A. Forticaux, L. Li, S. Jin, *J. Am. Chem. Soc.* **2013**, *135*, 10274-10277; b) D. Voiry, M. Salehi, R. Silva, T. Fujita, M. Chen, T. Asefa, V. B. Shenoy, G. Eda, M. Chhowalla, *Nano Lett.* **2013**, *13*, 6222-6227; c) D. Voiry, H. Yamaguchi, J. Li, R. Silva, D. C. B. Alves, T. Fujita, M. Chen, T. Asefa, V. B. Shenoy, G. Eda, M. Chhowalla, *Nat. Mater.* **2013**, *12*, 850-855; d) S. Peng, L. Xi, X. Han, W. Sun, M. Srinivasan, S. G. Mhaisalkar, F. Cheng, Q. Yan, J. Chen, S. Ramakrishna, *Angew. Chem. Int. Ed.* **2014**, *53*, 12594-12599; e) D. Voiry, R. Fullon, J. Yang, E. S. C. de Carvalho Castro, R. Kappera, I. Bozkurt, D. Kaplan, M. J. Lagos, P. E. Batson, G. Gupta, A. D. Mohite, L. Dong, D. Er, V. B. Shenoy, T. Asefa, M. Chhowalla, *Nat. Mater.* **2016**, *15*, 1003-1009; f) C. Tan, H. Zhang, *Chem. Soc. Rev.* **2015**, *44*, 2713-2731; g) H. Sun, X. Xu, Z. Yan, X. Chen, F. Cheng, P. Weiss, J. Chen, *Chem. Mater.* **2017**, *29*, 8539-8547.

[8] Z. Zeng, Z. Yin, X. Huang, H. Li, Q. He, G. Lu, F. Boey, H. Zhang, *Angew. Chem. Int. Ed.* **2011**, *50*, 11093-11097.

[9] H. Tang, J. Wang, H. Yin, H. Zhao, D. Wang, Z. Tang, *Adv. Mater.* **2015**, 27, 1117-1123.

[10] J. Jiang, M. Gao, W. Sheng, Y. Yan, *Angew. Chem.* **2016**, 55, 15240-15245.

[11] a) H. B. Li, M. H. Yu, F. X. Wang, P. Liu, Y. Liang, J. Xiao, C. X. Wang, Y. X. Tong, G. W. Yang, *Nat. Commun.* **2013**, 4, 1894; b)

[12] a) C. Yuan, J. Li, L. Hou, X. Zhang, L. Shen, X. W. D. Lou, *Adv. Funct. Mater.* **2012**, 22, 4592-4597; b) H. Yin, L. Jiang, P. Liu, M. Al-Mamun, Y. Wang, Y. L. Zhong, H. Yang, D. Wang, Z. Tang, H. Zhao, *Nano Res.* **2017**, DOI: https://doi.org/10.1007/s12274-017-1886-7.

[13] S. Zhang, H. C. Zeng, *Chem. Mater.* **2009**, 21, 871-883.

[14] J. Xie, H. Zhang, S. Li, R. Wang, X. Sun, M. Zhou, J. Zhou, X. W. D. Lou, Y. Xie, *Adv. Mater.* **2013**, 25, 5807-5813.

[15] J. Staszak-Jirkovsky, C. D. Malliakas, P. P. Lopes, N. Danilovic, S. S. Kota, K. C. Chang, B. Genorio, D. Strmcnik, V. R. Stamenkovic, M. G. Kanatzidis, N. M. Markovic, *Nat. Mater.* **2016**, 15, 197-203.

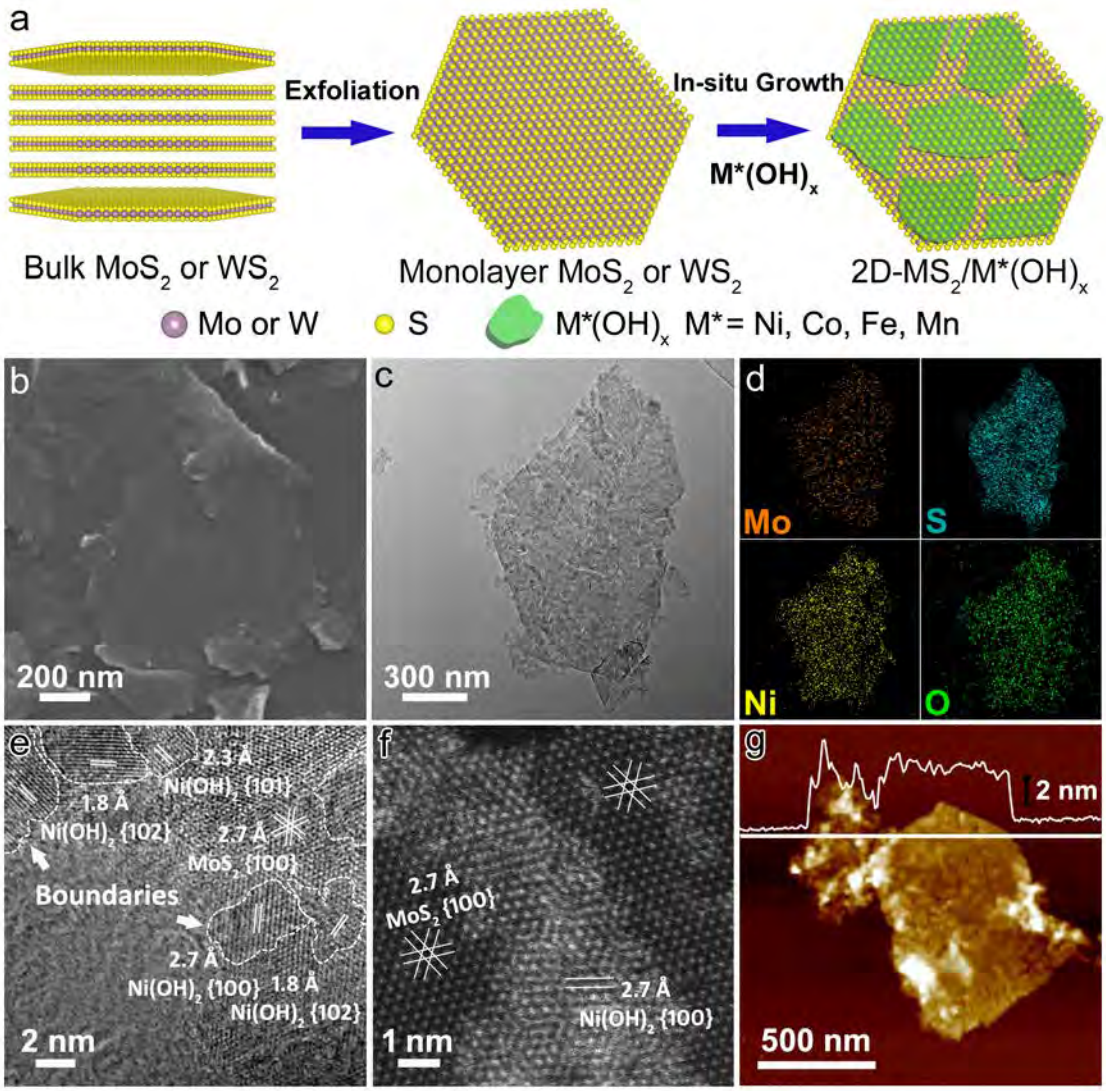

Figure 1. a) Schematic illustration of synthesis procedure of 2D-MS_2/M*$(OH)_x$ nanosheet; **b-g)** Structure of 2D-MoS_2/$Ni(OH)_2$-10: **b)** SEM, **c)** TEM image and **d)** EDS mapping of Mo, S, Ni and O elements of 2D-MoS_2/$Ni(OH)_2$-10; **e)** HRTEM, **f)** Atomic-resolution HAADF-STEM and **g)** AFM images of 2D-MoS_2/$Ni(OH)_2$-10

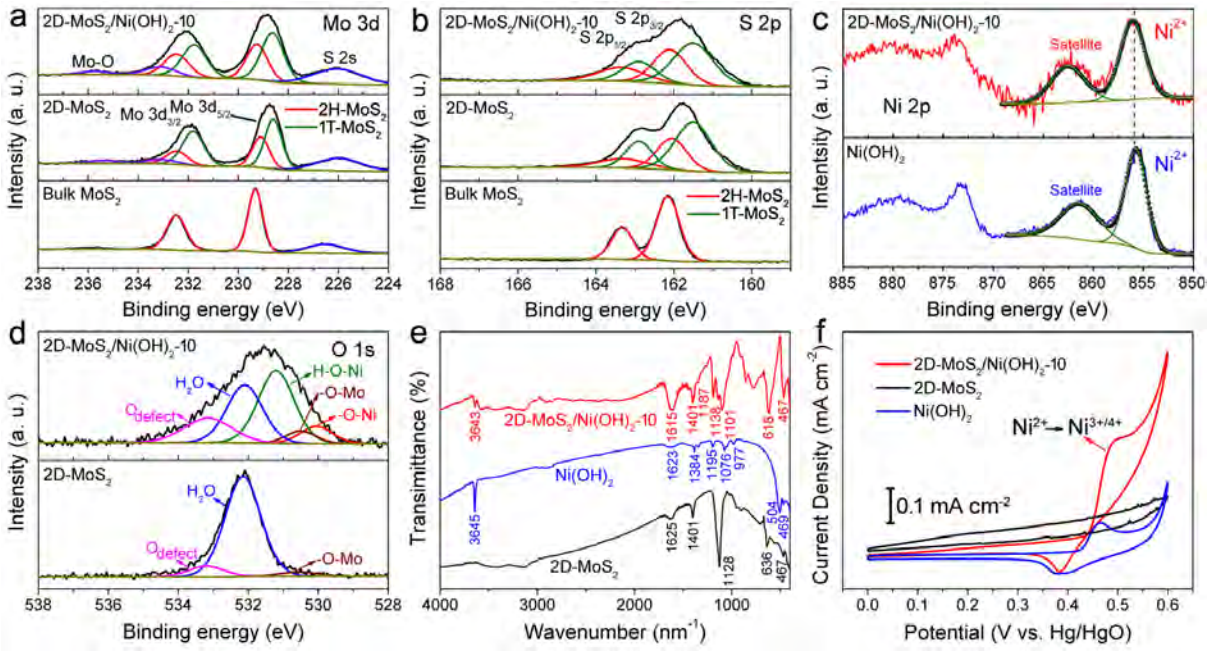

Figure 2. XPS spectra of **a)** Mo 3d and **b)** S 2p region of 2D-MoS_2/$Ni(OH)_2$-10, monolayer MoS_2 (2D-MoS_2) and bulk MoS_2; **c)** XPS spectra of Ni 2p region of 2D-MoS_2/$Ni(OH)_2$-10 and $Ni(OH)_2$; **d)** XPS spectra of O 1s region of 2D-MoS_2/$Ni(OH)_2$-10 and monolayer MoS_2; **e)** FTIR spectra and **f)** CV curves of 2D-MoS_2/$Ni(OH)_2$-10, 2D-MoS_2 and $Ni(OH)_2$ in 1 M KOH with scanning rate of 20 mV s^{-1}

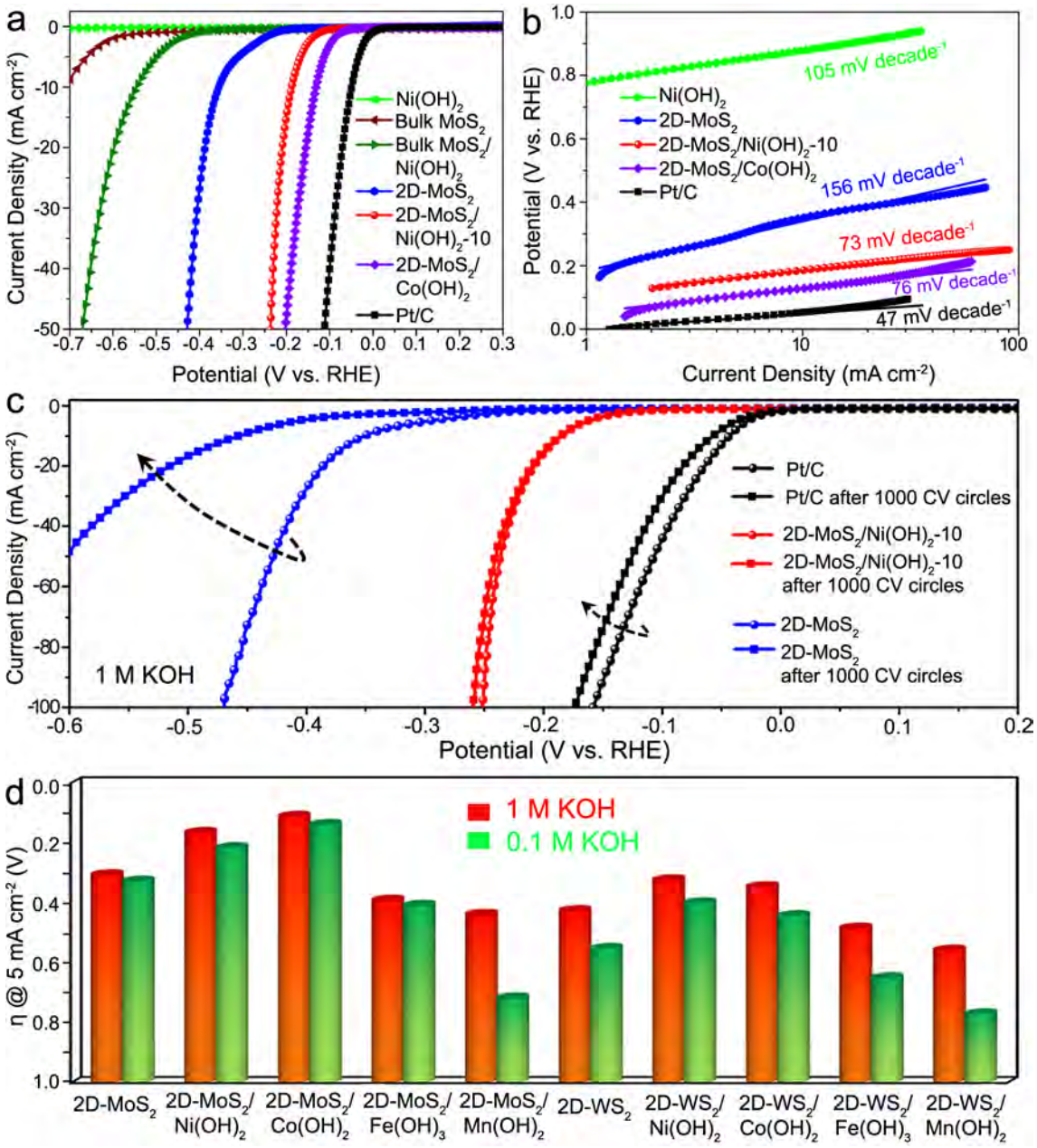

Figure 3.a) Alkaline HER performance; **b)** Corresponding Tafel slopes; **c)** Stabilities (Scan rate: 100 mV s^{-1}) of 2D-MoS_2/$Ni(OH)_2$-10, 2D-MoS_2/$Co(OH)_2$, bare 2D-MoS_2, $Ni(OH)_2$ and commercial Pt/C (20 wt.% Pt) in 1 M KOH. **d)** Trend in HER overpotential as a function of the as-synthesized hybrids and bare TMD nanosheets (expressed as η required for a 5 mA cm^{-2} current density in 0.1 M and 1 M KOH).

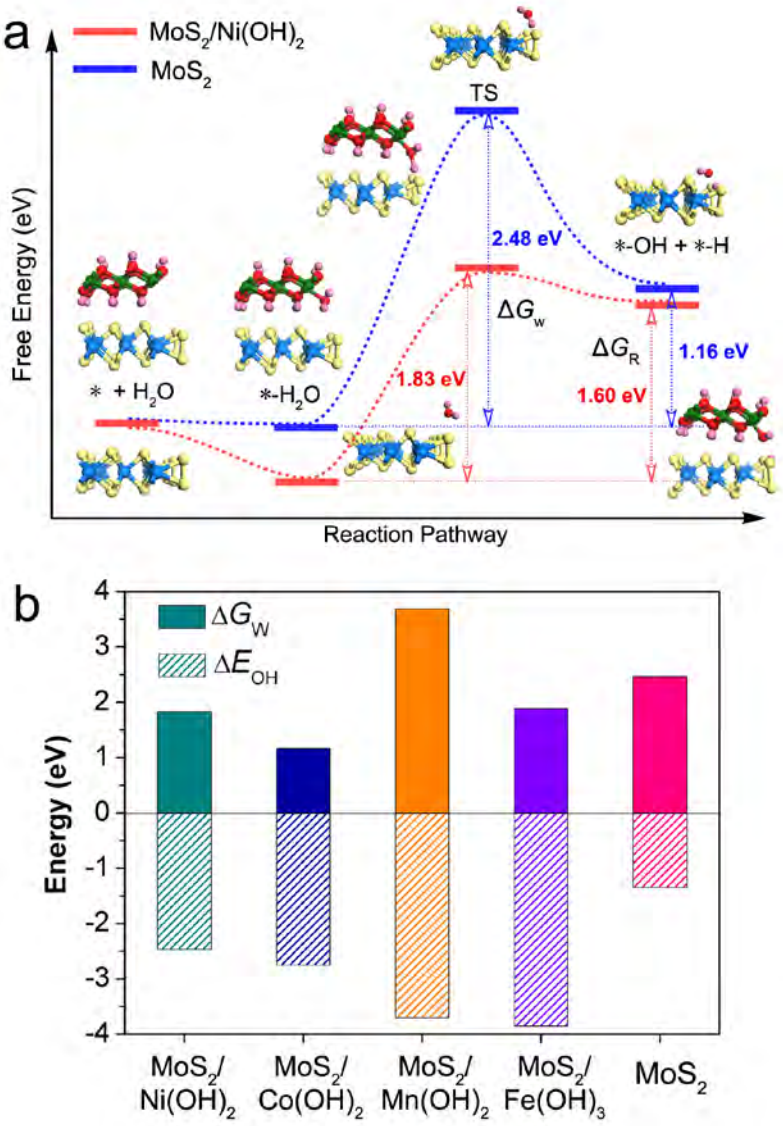

Figure 4. a) Free energy diagram of the water dissociation step for 2D-MoS_2 and 2D-MoS_2/$Ni(OH)_2$ hybrid with atomic configurations of reactant initial state, intermediate state, final state, and transition state. ΔG_R indicates the free energy change of the reaction, and ΔG_W indicates water dissociation kinetic energy barrier. Color codes: Mo, light blue; S, yellow; Ni, green; O, red; H, pink. **b)** ΔG_W and the chemisorption energies of hydroxides (ΔE_{OH}) on bare 2D-MoS_2 and various 2D-MoS_2/M*$(OH)_x$ heterostructure.

2D electrocatalysts: Ultrathin 2D hybrids are designed and prepared *via* surface modification of monolayer MoS_2 and WS_2 nanosheets by metal (Ni, Co, Fe, Mn) hydroxides, which form a new class of alkaline HER electrocatalysts. Among them, 2D-MoS_2/$Co(OH)_2$ heterostructure shows an extremely low HER overpotential of *ca.* 128 mV at 10 mA cm^{-2} in 1 M KOH. The surface introduction of metal hydroxides can effectively reduce the kinetic energy barrier of prior water dissociation step.

Keyword: Electrocatalysis, 2D materials, Hydrogen Evolution Reaction, Transition Metal Dichalcogenide, Metal Hydroxide

Zhengju Zhu, Huajie Yin,* Chun-Ting He, Mohammad Al-Mamun, Porun Liu, Lixue Jiang, Yong Zhao, Yun Wang, Hua Gui Yang, Zhiyong Tang, Dan Wang, Xiao-Ming Chen and Huijun Zhao*

Ultrathin Transition Metal Dichalcogenide/*3d* Metal Hydroxide Hybridized Nanosheets to Enhance Hydrogen Evolution Activity

ToC figure

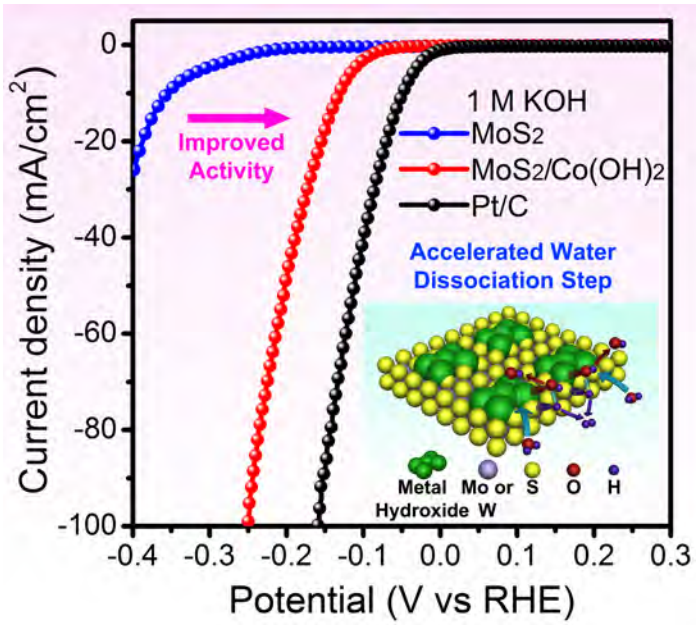

((Supporting Information can be included here using this template))

Supporting Information

Ultrathin Transition Metal Dichalcogenide/*3d* Metal Hydroxide Hybridized Nanosheets to Enhance Hydrogen Evolution Activity

Zhengju Zhu, Huajie Yin, Chun-Ting He, Mohammad Al-Mamun, Porun Liu, Lixue Jiang, Yong Zhao, Yun Wang, Hua Gui Yang, Zhiyong Tang, Dan Wang and Xiao-Ming Chen, Huijun Zhao**

Experimental details

Chemicals. Hexamethylenetetramine (HMT, 99.9%, AR grade) was purchased from Chemical-Supply. All other chemicals and reagents were bought from Sigma-Aldrich and used directly without further purification. Ultrapure water (Millipore Milli-Q grade) with a resistivity of 18.2 MΩ was used in all experiments.

Synthesis of MoS_2 nanosheets. 0.5 g of natural MoS_2 crystals were immersed in 10 mL of 2.5 M n-butyl-lithium solution in hexane for 3 days in a flask filled with argon gas. As-synthesized Li_xMoS_2 was retrieved by filtration and washed with hexane to remove excessive Li and organic residues. Then, exfoliation was performed within 30 mins by ultrasonicating Li_xMoS_2 in 1.0 L water for 2 h. The mixture was centrifuged several times to remove excessive lithium in the form of LiOH and unexfoliated materials. The concentration of the exfoliated MoS_2 solution was ~0.3 mg ml^{-1}. Typical SEM and TEM images are shown in Figure S1.

Synthesis of 2D-MoS_2/$Ni(OH)_2$-n. In a typical process, 60 mL solution containing 0.3 mg ml^{-1} MoS_2 after purged by nitrogen was mixed with different amount of $Ni(NO_3)_2 \cdot 6H_2O$ including 5 mg, 10 mg, 20 mg, 40 mg and 60 mg. Then 200 mg HMT was added into the above solution. After stirring for 60 minutes to dissolve completely, the mixed solution was

transferred into a 100 ml Teflon-lined autoclave, which was sealed and heated in an oven at 120 °C for 24 h and then cooled to room temperature naturally. The resulting black product was collected by centrifugation, then washed several times by distilled water and absolute ethanol to remove ions and possible remnants, and dried using freezing dryer.

Synthesis of 2D-MoS_2/$Co(OH)_2$. The synthetic procedure was similar to that of 2D-MoS_2/$Ni(OH)_2$ hybrids except that the $Ni(NO_3)_2{\cdot}6H_2O$ was replaced by the $Co(NO_3)_2{\cdot}6H_2O$.

Synthesis of 2D-MoS_2/$Fe(OH)_3$. 2D-MoS_2/$Fe(OH)_3$ hybrids were under ambient atmospheric conditions. First, 60 ml MoS_2 solution was purged by pure nitrogen for 1 hour. Then, 0.1 ml ferric chloride ($FeCl_3$) solution (100 mg $FeCl_3{\cdot}6H_2O$ in 1 ml water) was injected into above MoS_2 solution. After stirring the mixture for 1 h, the mixed solution was centrifuged to remove supernatant and obtained precipitates were re-dispersed into 20 ml water again. Into this solution, 20 ml 0.1 M KOH solution was added under suitable stirring. After reaction for 3 h under ambient atmospheric conditions, the final black product was collected by centrifugation, then washed with distilled water and ethanol, and dried using freezing dryer.

Synthesis of 2D-MoS_2/$Mn(OH)_2$. The synthetic procedure was similar to that of 2D-MoS_2/$Fe(OH)_3$ hybrids except that the $FeCl_3{\cdot}6H_2O$ was replaced by the $MnCl_2{\cdot}4H_2O$.

Synthesis of bare 2D-MoS_2, $Ni(OH)_2$ and $Co(OH)_2$. For comparison, bare 2D-MoS_2 was synthesized through similar process like 2D-MoS_2/$Ni(OH)_2$ without involving $Ni(NO_3)_2{\cdot}6H_2O$. And pure $Ni(OH)_2$ and $Co(OH)_2$ was prepared replacing MoS_2 solution with distilled water.

Synthesis of WS_2 nanosheets. 1.0 g of natural WS_2 crystals were put in a 50 ml Teflon-lined autoclave and 5 mL of 2.5 M n-butyllithium solution was added into the autoclave. Then the solution was diluted to 0.5 M with hexane. After that, the autoclave was heated at 80 °C for 24 h and then cooled to room temperature naturally. All above preparation was carried out in a glove box in an Argon atmosphere. Subsequently, exfoliation was performed within 30 mins by ultrasonicating Li_xWS_2 in 1.0 L water for 2 h. Washing with distilled water and ethanol via

centrifuging was also performed to remove LiOH and unexfoliated materials. The concentration of the exfoliated WS_2 solution was ~0.2 mg ml^{-1}. Typical SEM and AFM images are shown in Figure S2.

Synthesis of 2D-WS_2/metal hydroxide hybrids. Four kinds of WS_2-based hybrids were prepared like 2D-MoS_2-based bybirds by using WS_2 solution instead of MoS_2.

Characterization. XRD patterns were obtained from a Shimadzu XRD-6000 diffractometer by scanning the angular range $10° \leq 2\theta \leq 80°$ using CuKα radiation (λ = 1.5418 Å). The microstructure of the powders was revealed observing Pt-coated samples under a Hitachi S7100 scanning electron microscopy (SEM). Transmission electron microscopy (TEM) and energy-dispersive X-ray spectroscopy (EDS) elemental mapping were performed on Philips F20 at 200 kV. High angle annular dark field scanning transmission electron microscope (HAADF-STEM) imaging was performed using a probe corrected JEOL JEM-ARM200F instrument with at an acceleration voltage of 200 kV. The X-ray photoelectron spectra (XPS) were recorded on a Kratos Axis ULTRA system. Fourier transform infrared spectra (FTIR) were measured on a Bruker Vector-22 FTIR spectrometer with a scan range of 400 cm^{-1} to 4000 cm^{-1}. Atomic force microscopy (AFM) measurements were implemented by Bruker Dimension Icon system. Raman spectra were taken using a RENISHAW mVia Raman microscope using a 532 nm excitation laser. UV-Vis absorption spectroscopy of smple dispersions in water were recorded using a Cary Series (Agilent Technologies) spectrophotometer. Thermogravimetric analysis (TGA) were performed on a NETZSCHSTA-449 TG Analyzer under the protection of argon with a heating rate of 10 °C min^{-1}.

Electrochemical measurements. The electrocatalyst ink was prepared as follows: 4 mg of electrocatalyst powder was dispersed in 950 μL isopropanol mixed solvent with 50 μl of Nafion solution, then the mixture was ultrasonicated for about 1 h to generate a homogeneous ink. Then 14 μl of the dispersion was transferred onto the glassy carbon electrode with diameter of 5 mm, leading to the electrocatalyst loading ~0.285 mg cm^{-2}. Finally, the

electrode was dried at room temperature. The electrochemical tests were performed in a three-electrode electrochemical cell (CHI 760D) using a graphite rod and a Hg/HgO electrode as the counter and reference electrode, respectively. Before the electrochemical measurement, the fresh electrolyte (0.1 M or 1 M KOH) was treated by bubbling pure N_2 for at least 30 min. The HER polarization curves were obtained by sweeping the potential from -0.5 to -1.7 V vs Hg/HgO with a sweep rate of 5 mV s^{-1} and a rotation rate of 1,600 r.p.m. The resistances of systems were recorded at -1.2 V versus Hg/HgO in all electrolytes, and all data were reported with iR compensation. For the stability evaluation, electrode potential was cycled from -0.6 to -1.6 V vs. Hg/HgO at a sweep rate of 100 mV s^{-1}. At the end of the cycling experiment, the HER polarization curves were obtained with a sweep rate of 5 mV s^{-1}. Electrochemical surface area (ECSA) of the electrocatalyst was estimated from the electrochemical double-layer capacitance of the catalytic surface according to T. F. Jaramillo's work (*J. Am. Chem. Soc.* **2013**, *135*, 16977). For our estimates of surface area, we use general specific capacitances of Cs = 0.040 mF cm^{-2} in 1 M KOH based on typical reported values.

TOF calculation. The turnover frequency (TOF) value was calculated by assuming all current is used to produce molecular H_2 with 100% Faraday efficiency. The equation adopted here was based on reported method (*J. Am. Chem. Soc.* **2015**, *137*, 4347).

$$\mathrm{TOF} = j \times \mathrm{S}/2\mathrm{F}n$$

where j (mA cm^{-2}) is the current density, S is the surface area of glassy carbon disk, F is the Faraday constant (96485 C mol^{-1}), and n is measured active sites that parcipitate in the reaction (the measurement method is according to Hu's report, *Chem. Sci.*, **2011**, *2*, 1262). All relevant data were listed in Table SE-1 below.

Table SE-1. Comparison of MoS_2-based hybrids in terms of MoS_2 content, Mo content, $M^*(OH)_x$ content, M* content, MoS_2 loading and active sites.

Name	MoS_2 (wt %)	Mo content (μmol cm^{-2})	$M^*(OH)_x$ (wt %)	M* content (μmol cm^{-2})	MoS_2 loading (mg cm^{-2})	Active sites (μmol cm^{-2})
$MoS_2/Mn(OH)_2$	81.65	1.45	18.35	0.59	0.233	0.054
$MoS_2/Fe(OH)_3$	83.32	1.48	16.68	0.45	0.237	0.048
MoS_2	100.00	1.78	0.00	0.00	0.285	0.074
$MoS_2/Ni(OH)_2$	85.39	1.52	14.61	0.45	0.243	0.051
$MoS_2/Co(OH)_2$	87.35	1.56	12.65	0.39	0.249	0.060

DFT calculation:

The spin polarization density functional theory (DFT) calculations were performed by the $Dmol^3$ module in Materials Studio 5.5 package, and generalized gradient approximation (GGA) with Perdew-Becke-Ernzerhof (PBE) was used for the exchange-correlation functional. The double numerical plus d-functions (DND) basis set were adopted, while an accurate DFT Semi-core Pseudopots (DSPP) was employed for the metal atoms. All of the models are calculated in periodically boxes with a vacuum slab of 18 Å to separate the interaction between periodic images. The transition state search was performs with an LST, followed by repeated conjugate gradient minimizations and QST maximizations until a transition state has been located. All the transition state configurations were confirmed through the frequency analysis. The energy, gradient and displacement convergence criterions were set as 1×10^{-5} Ha, 2×10^{-3} Å and 5×10^{-3} Å, respectively.

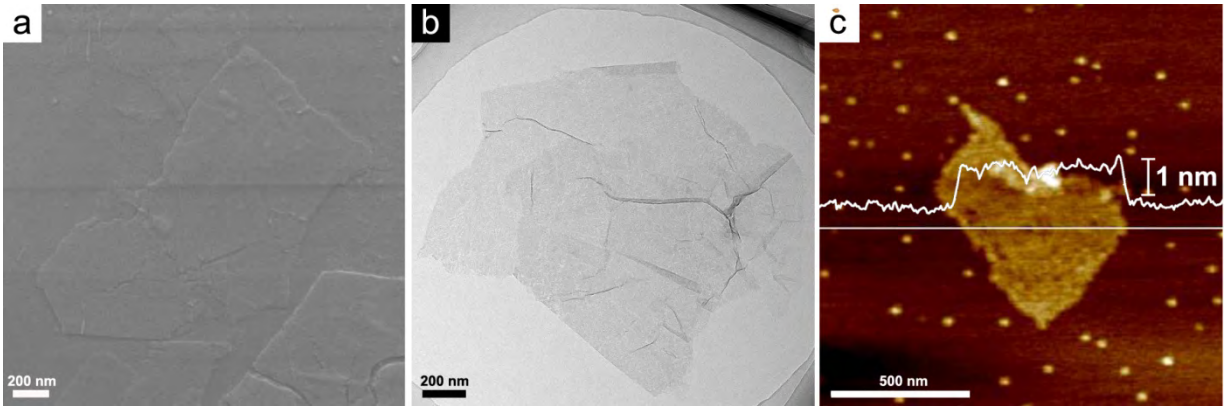

Figure S1. (**a**) SEM image of exfoliated monolayer MoS_2 nanosheets. (**b**) TEM image of exfoliated MoS_2 nanosheets. (**c**) AFM image of MoS_2 nanosheet deposited on mica.

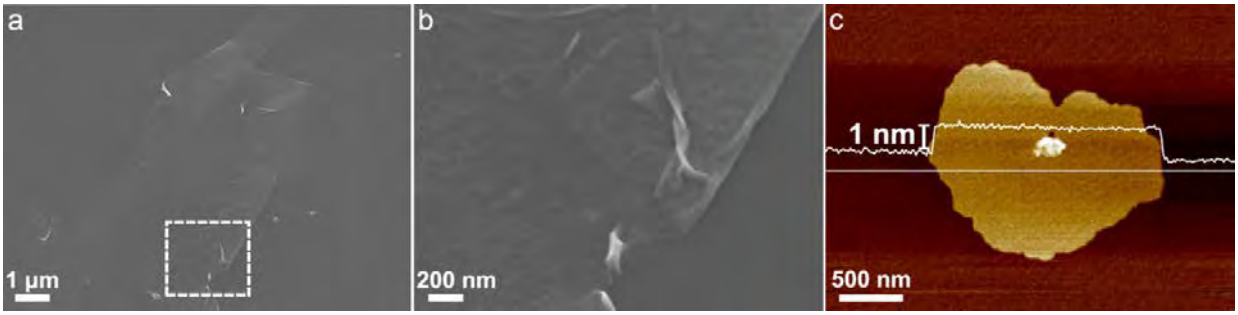

Figure S2. (**a,b**) SEM images of exfoliated WS_2 nanosheets, and (**b**) shows SEM image of enlarged area (while square) in (**a**). (**c**) AFM image of WS_2 nanosheet deposited on mica.

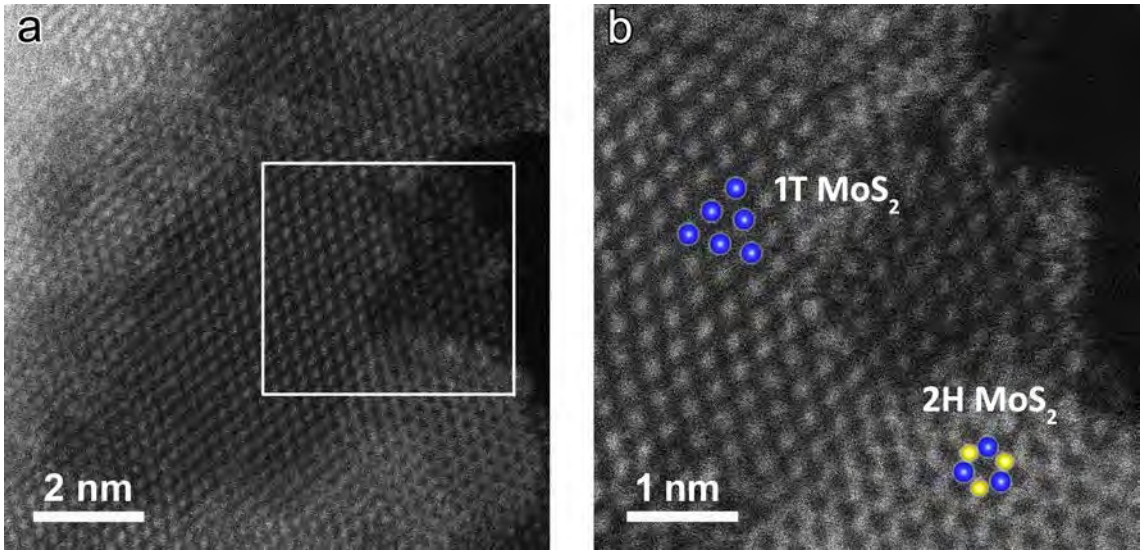

Figure S3. Addtional HAADF-STEM images of 2D-MoS_2/$Ni(OH)_2$-10

The detailed atomistic arrangements of the metallic 1T phase (**trigonal lattice area** of octahedral coordination) and semiconducting 2H phase (**honeycomb lattice area of the trigonal prismatic coordination**) can be clearly visualized in the selected enlarged area in this typical HAADF-STEM image (*ACS Nano* **2012**, *6*, 7311; *J. Am. Chem. Soc*. **2015**, *137*, 2622), confirming the co-existence of 1T and 2H phases in our hybrid nanosheets.

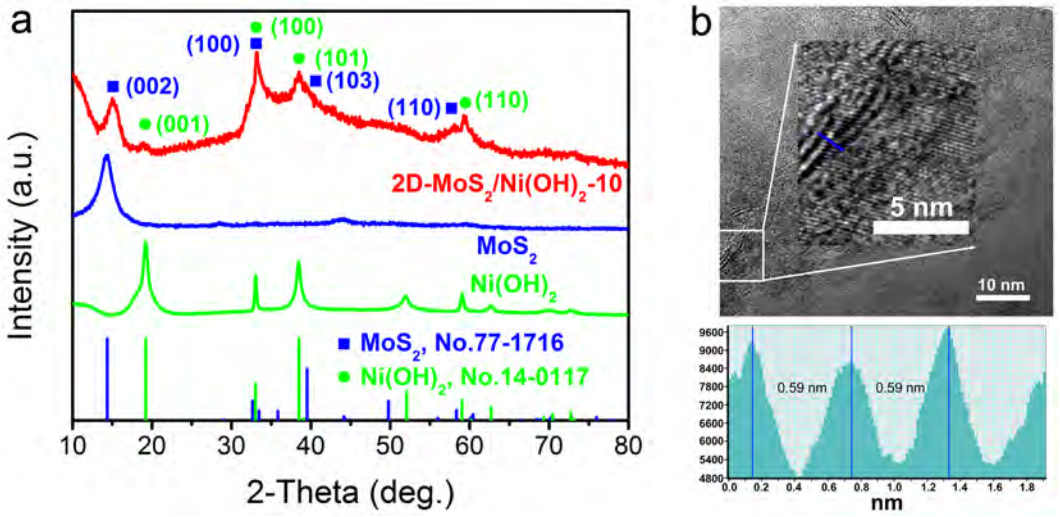

Figure S4. (a) XRD patterns of 2D-MoS_2/$Ni(OH)_2$-10, 2D-MoS_2 and $Ni(OH)_2$. (b) HRTEM image of 2D-MoS_2/$Ni(OH)_2$-10 wiht corresponding line profiling. The region indicated by the square is enlarged to show the layered structure of 2D-MoS_2. Line scan of the HRTEM image indicated by the blue lines, indicating a layer-to-layer spacing of 0.59 nm, agreeing well with XRD results.

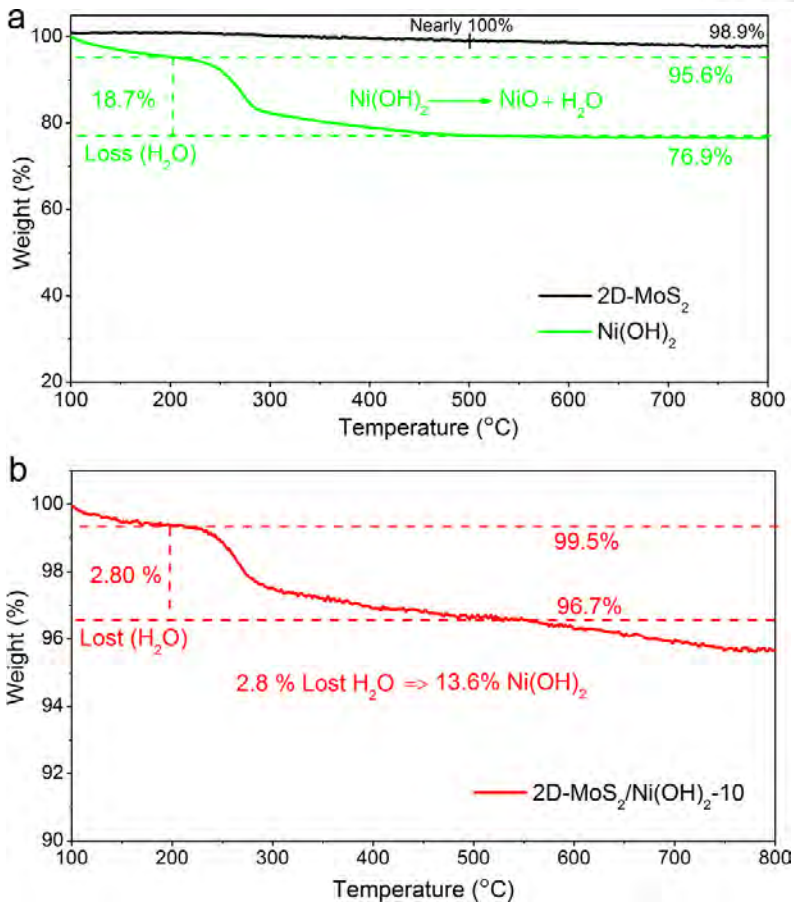

Figure S5. (**a**) TGA curves of bare 2D-MoS_2 and $Ni(OH)_2$; (**b**) TGA curve of 2D-MoS_2/$Ni(OH)_2$-10.

The TGA curve of β-$Ni(OH)_2$ (**Figure S5a**) showed a weight loss of 18.7% in the temperature range of 200-500 °C, which is almost identical to the calculated weight loss of 19.4% due to one H_2O lose from $Ni(OH)_2$ to form NiO. While 2D MoS_2 (**Figure S5a**) can retain near 100% of its original weight before 500 °C and 98.9% up to 800 °C, which is consistent with TGA results of the ultrathin MoS_2 nanosheets reported by Xie *et al* (*J. Am. Chem. Soc.* **2013**, *135*, 17881). The TGA curve of 2D-MoS_2/$Ni(OH)_2$-10 hybrid (**Figure S5b**) revealed a weight decrease of 2.8% during the conversion of $Ni(OH)_2$ to NiO in a temperature range of 200-500 °C. The small weight loss is due to the loss of water contents. Based on the TGA data, the weight percentage of $Ni(OH)_2$ in 2D-MoS_2/$Ni(OH)_2$-10 is ~13.6%, in a good agreement with the ICP determined weight percentage of 15.6 wt.%.

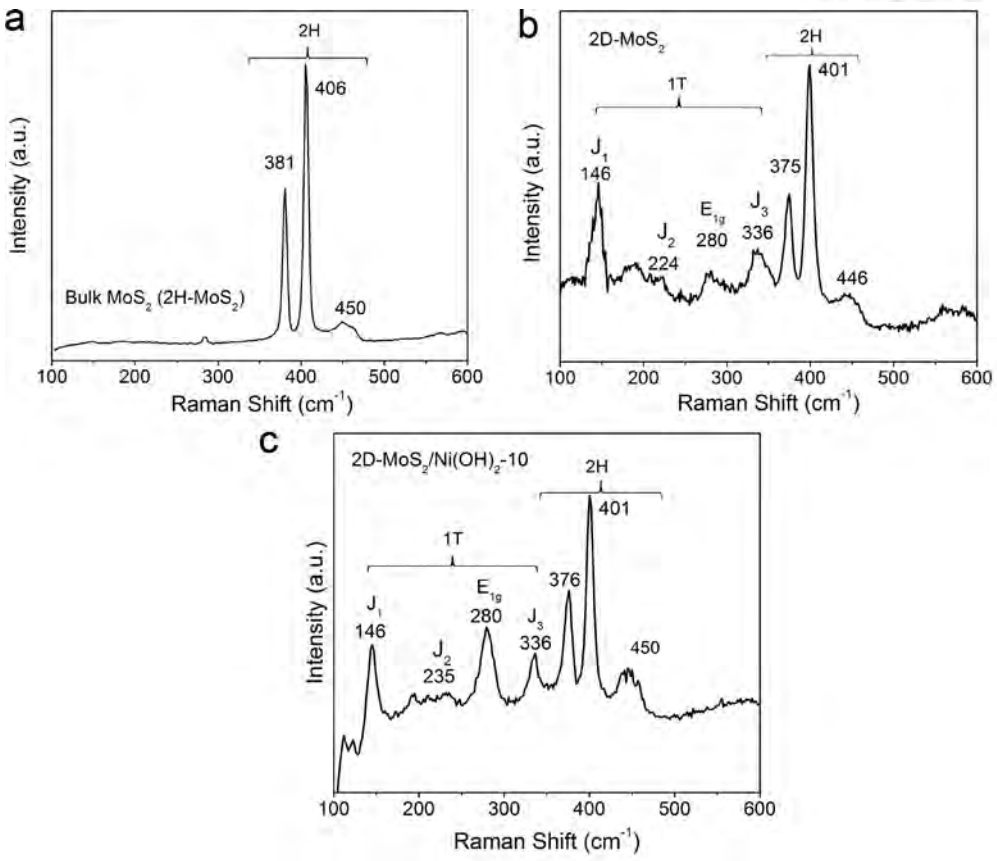

Figure S6. Raman spectra of (**a**) bulk MoS_2, (**b**) 2D-MoS_2, (**c**) 2D-MoS_2/$Ni(OH)_2$-10

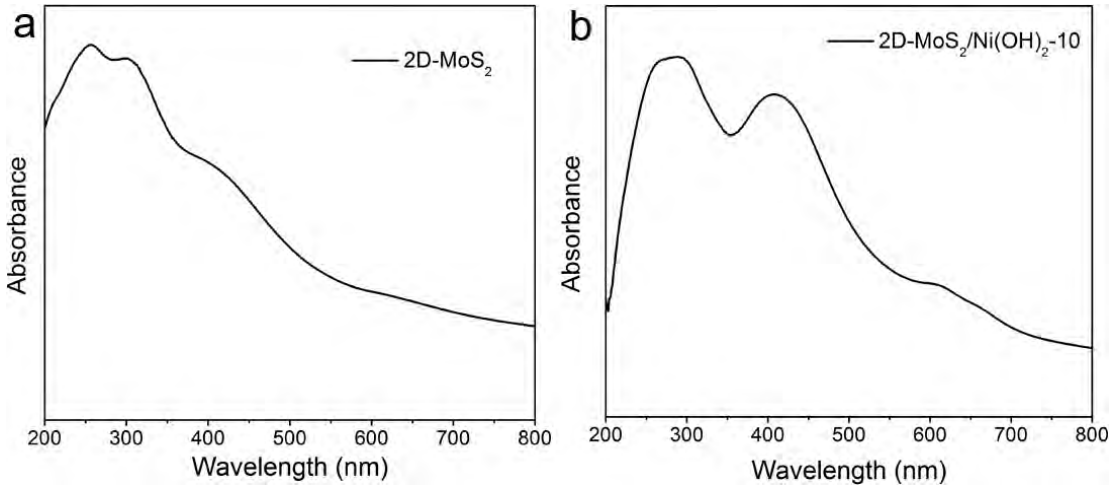

Figure S7. (**a-c**) UV-vis spectra of 2D-MoS_2 and 2D-MoS_2/$Ni(OH)_2$-10

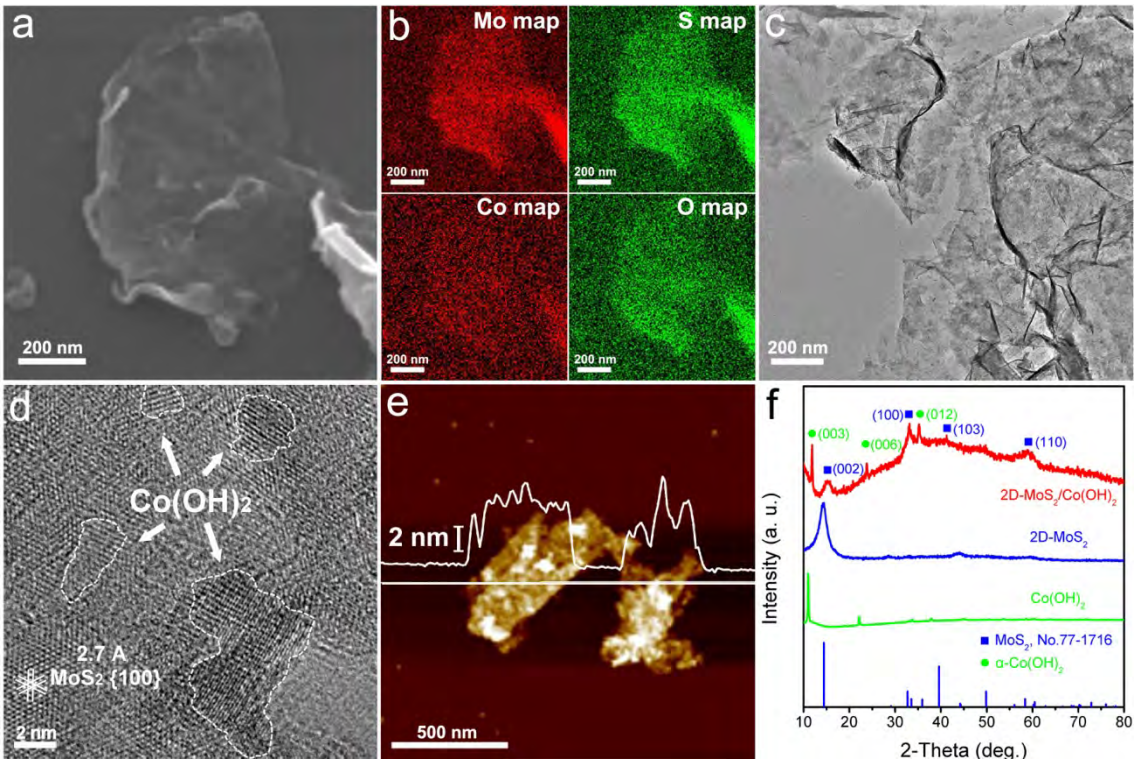

Figure S8. (**a**) SEM image of 2D-MoS_2/$Co(OH)_2$ and its corresponding (**b**) Mo EDS mapping, S EDS mapping, Co EDS mapping and O EDS mapping. (**c**,**d**) TEM images of 2D-MoS_2/$Co(OH)_2$. (**e**) AFM image of 2D-MoS_2/$Co(OH)_2$ deposited on mica. (**f**) XRD patterns of 2D-MoS_2/$Co(OH)_2$, 2D-MoS_2 and $Co(OH)_2$

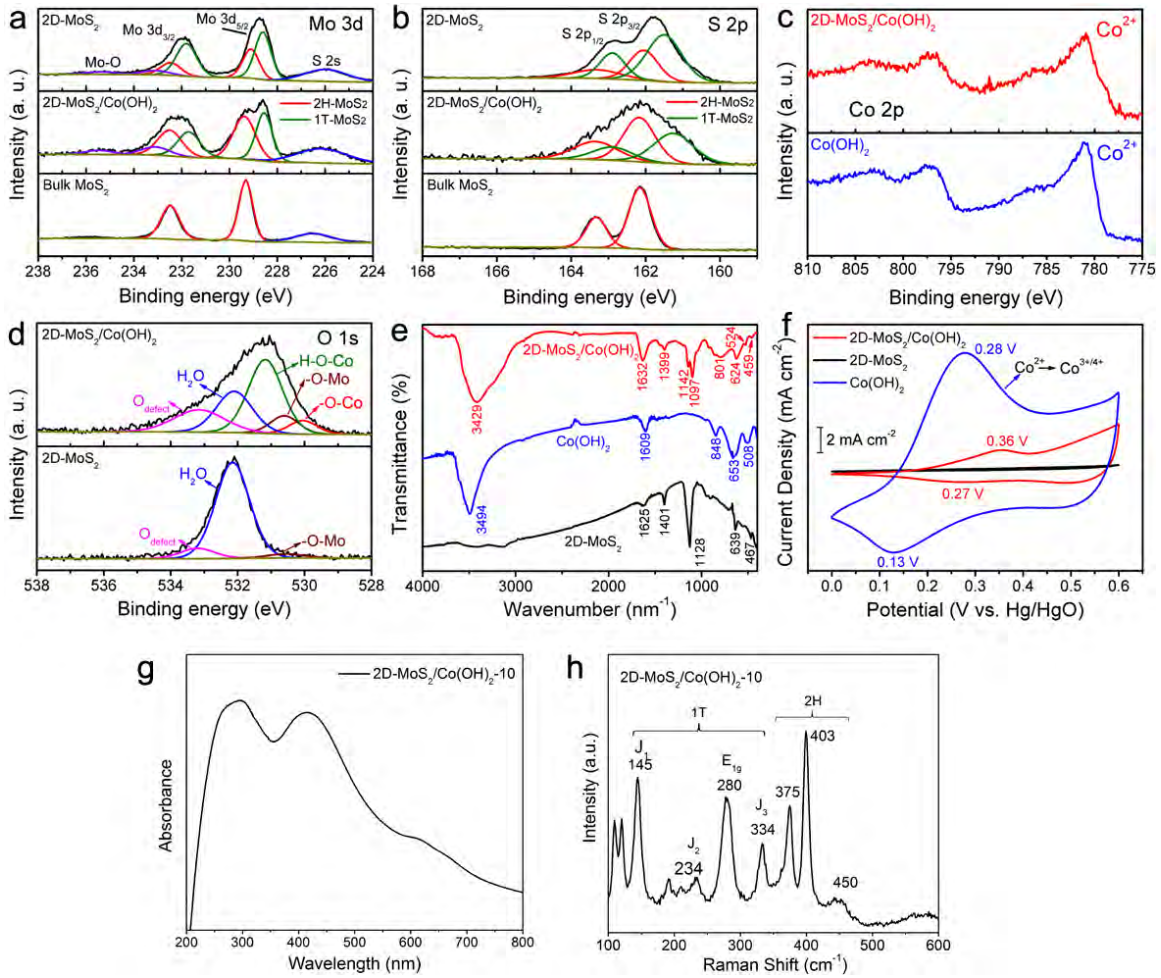

Figure S9. Comparison of XPS spectra of 2D-MoS_2, 2D-MoS_2/$Co(OH)_2$ and bulk MoS_2 in the (**a**) Mo 3d and (**b**) S 2p regions. XPS spectra of 2D-MoS_2/$Co(OH)_2$ and $Co(OH)_2$ in the (**c**) Co 2p. XPS spectra of 2D-MoS_2/$Co(OH)_2$ and 2D-MoS_2 in the (**d**) O 1s. (**e**) FTIR spectra of 2D-MoS_2/$Co(OH)_2$, $Co(OH)_2$ and 2D-MoS_2. (**f**) CV curves of 2D-MoS_2/$Co(OH)_2$, 2D-MoS_2 and $Co(OH)_2$ in the region of 0-0.6 V vs. Hg/HgO at 20 mV s^{-1} scan rate in the 1 M KOH; (g) UV-vis spectrum and (h) Raman of 2D-MoS_2/$Co(OH)_2$.

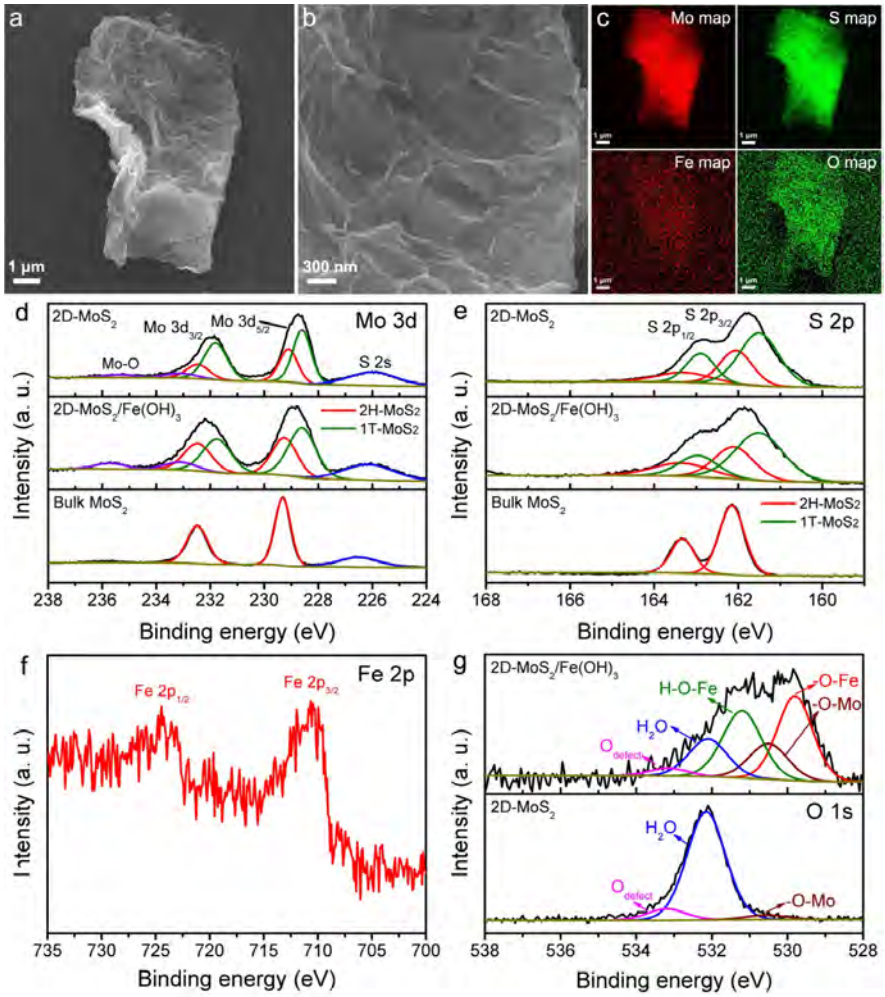

Figure S10. (**a**,**b**) SEM images of 2D-MoS_2/$Fe(OH)_3$ and corresponding (**c**) Mo EDS mapping, S EDS mapping, Fe EDS mapping and O EDS mapping in (**a**). Comparison of XPS spectra of MoS_2, MoS_2/$Fe(OH)_3$ and bulk MoS_2 in the (**d**) Mo 3d and (**e**) S 2p regions. XPS spectra of MoS_2/$Fe(OH)_3$ in the (**f**) Fe 2p. XPS spectra of 2D-MoS_2/$Fe(OH)_3$ and 2D-MoS_2 in the (**g**) O 1s.

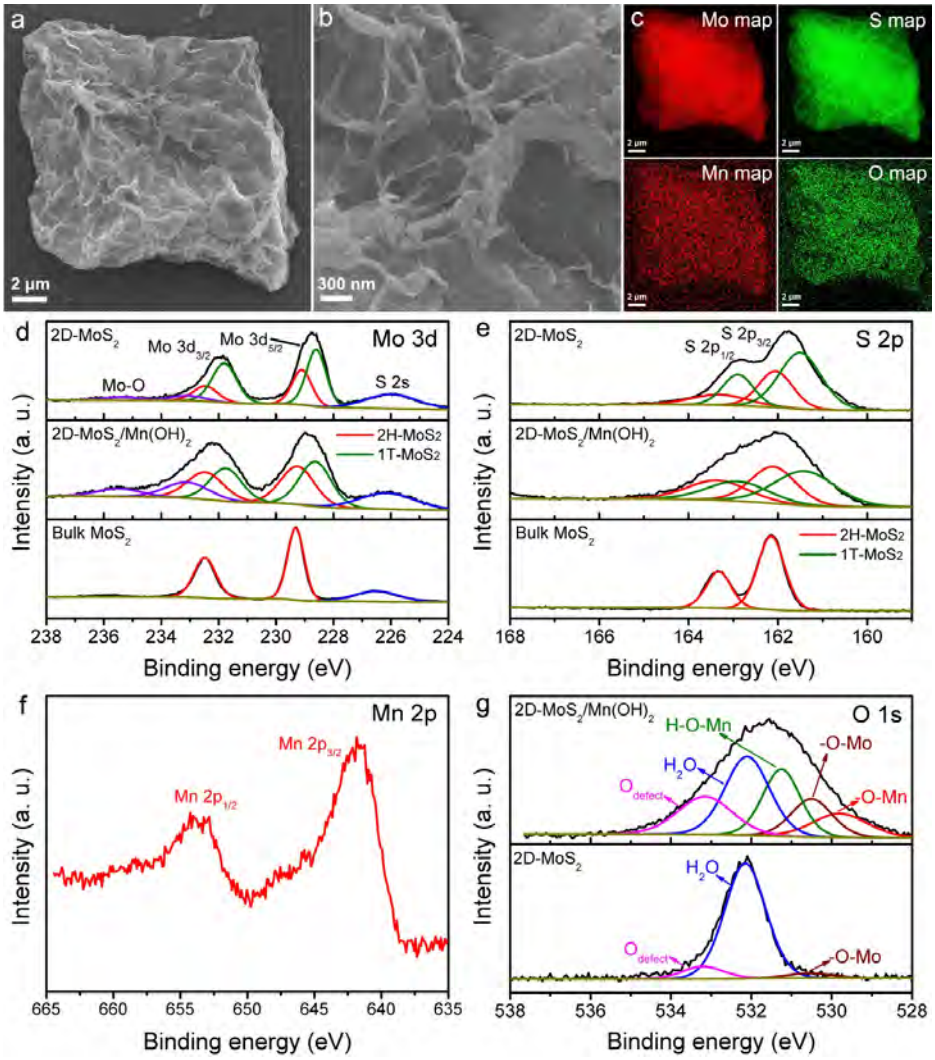

Figure S11. (**a**,**b**) SEM images of 2D-MoS_2/$Mn(OH)_2$ and corresponding (**c**) Mo EDS mapping, S EDS mapping, Mn EDS mapping and O EDS mapping in (**a**). Comparison of XPS spectra of 2D-MoS_2, 2D-MoS_2/$Mn(OH)_2$ and bulk MoS_2 in the (**d**) Mo 3d and (**e**) S 2p regions. XPS spectra of 2D-MoS_2/$Mn(OH)_2$ in the (**f**) Mn 2p. XPS spectra of 2D-MoS_2/$Mn(OH)_2$ and 2D-MoS_2 in the (**g**) O 1s.

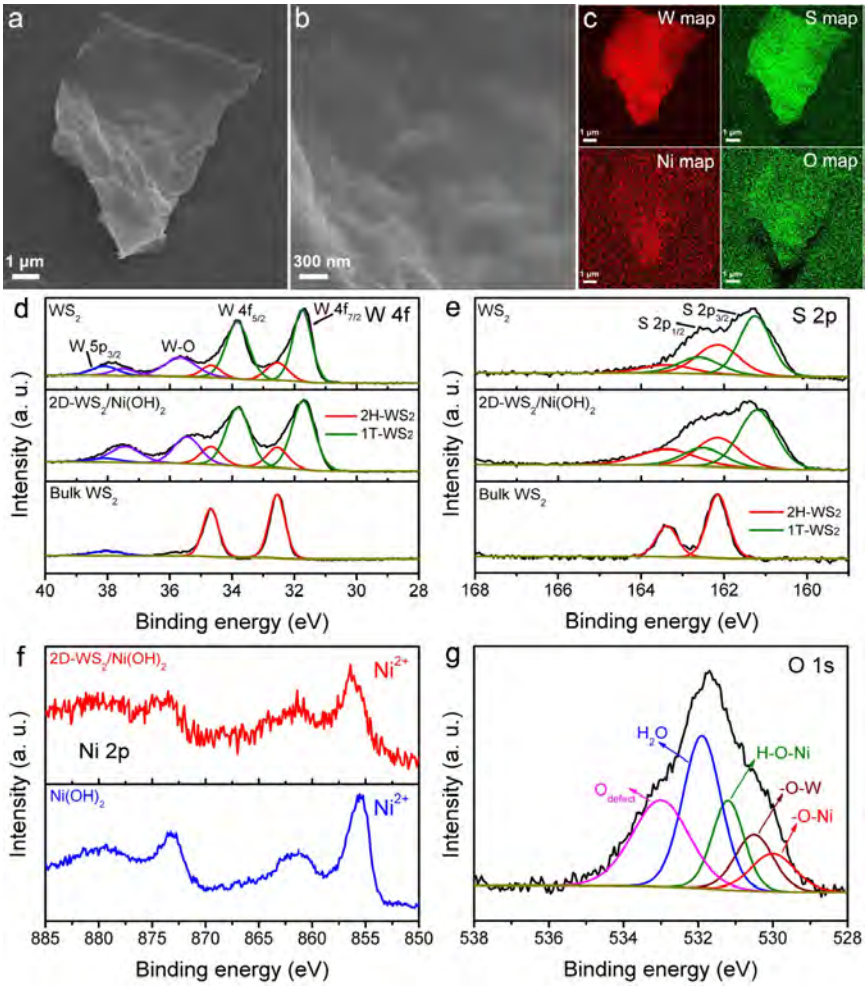

Figure S12. (**a**,**b**) SEM images of 2D-WS_2/$Ni(OH)_2$ and corresponding (**c**) W EDS mapping, S EDS mapping, Ni EDS mapping and O EDS mapping in (**a**). Comparison of XPS spectra of 2D-WS_2, 2D-WS_2/$Ni(OH)_2$ and bulk WS_2 in the (**d**) W 4f and (**e**) S 2p regions. XPS spectrum of 2D-WS_2/$Ni(OH)_2$ and $Ni(OH)_2$ in the (**f**) Ni 2p. XPS spectra of 2D-WS_2/$Ni(OH)_2$ in the **(g)** O 1s.

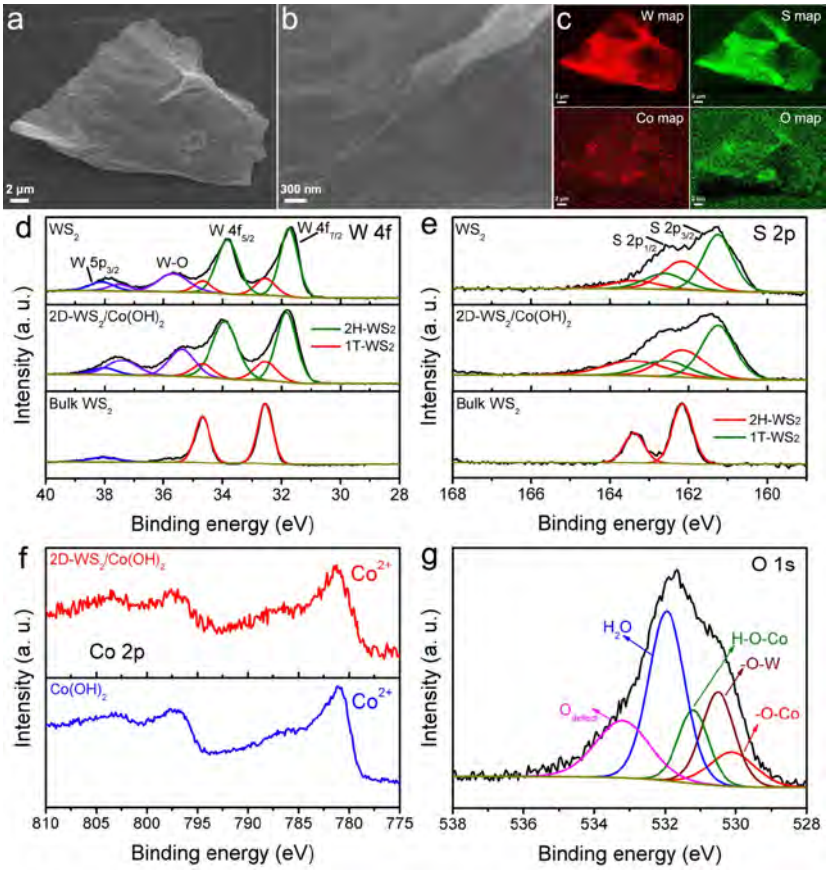

Figure S13. (**a**,**b**) SEM images of 2D-WS_2/$Co(OH)_2$ and corresponding (**c**) W EDS mapping, S EDS mapping, Co EDS mapping and O EDS mapping in (**a**). Comparison of XPS spectra of 2D-WS_2, 2D-WS_2/$Co(OH)_2$ and bulk WS_2 in the (**d**) W 4f and **(e)** S 2p regions. XPS spectrum of 2D-WS_2/$Co(OH)_2$ and $Co(OH)_2$ in the (**f**) Co 2p. XPS spectra of 2D-WS_2/$Co(OH)_2$ in the (**g**) O 1s.

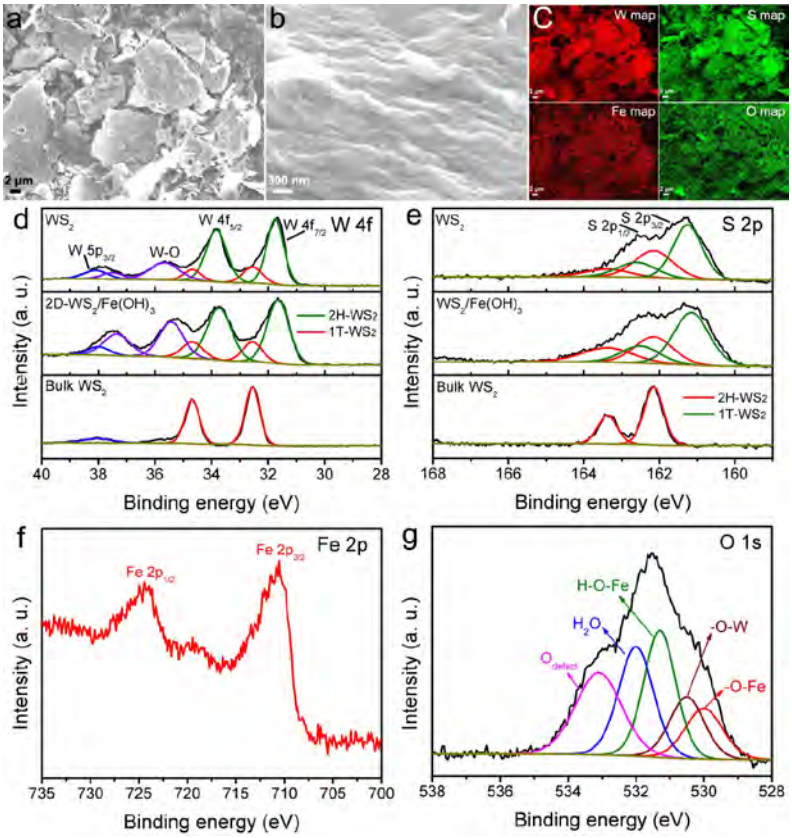

Figure S14. (**a**,**b**) SEM images of 2D-WS_2/$Fe(OH)_3$ and corresponding (**c**) W EDS mapping, S EDS mapping, Fe EDS mapping and O EDS mapping in (**a**). Comparison of XPS spectra of 2D-WS_2, 2D-WS_2/$Fe(OH)_3$ and bulk WS_2 in the (**d**) W 4f and (**e**) S 2p regions. XPS spectrum of 2D-WS_2/$Fe(OH)_3$ in the (**f**) Fe 2p. XPS spectra of 2D-WS_2/$Fe(OH)_3$ in the (**g**) O 1s.

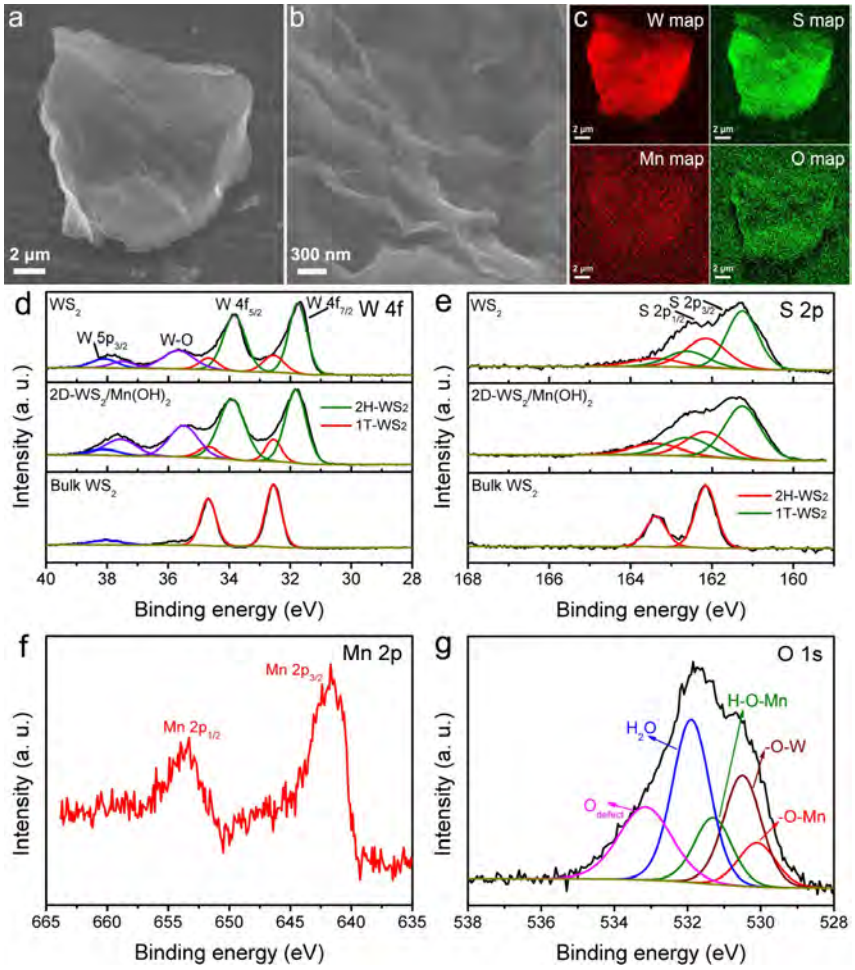

Figure S15. (**a**,**b**) SEM images of 2D-WS_2/$Mn(OH)_2$ and corresponding (**c**) W EDS mapping, S EDS mapping, Mn EDS mapping and O EDS mapping in (**a**). Comparison of XPS spectra of 2D-WS_2, 2D-WS_2/$Mn(OH)_2$ and bulk WS_2 in the (**d**) W 4f and (**e**) S 2p regions. XPS spectrum of 2D-WS_2/$Mn(OH)_2$ in the (**f**) Mn 2p. XPS spectra of 2D-WS_2/$Mn(OH)_2$ in the (**g**) O 1s.

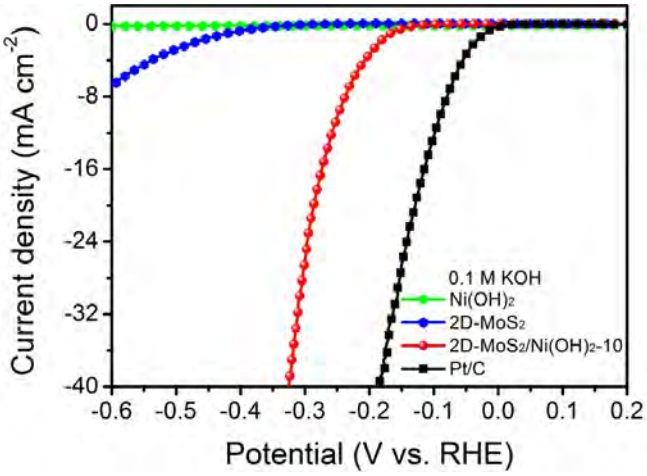

Figure S16. Alkaline HER performance of 2D-MoS_2/$Ni(OH)_2$-10, bare 2D-MoS_2, $Ni(OH)_2$ and commercial Pt/C (20 wt.% Pt) in 0.1 M KOH.

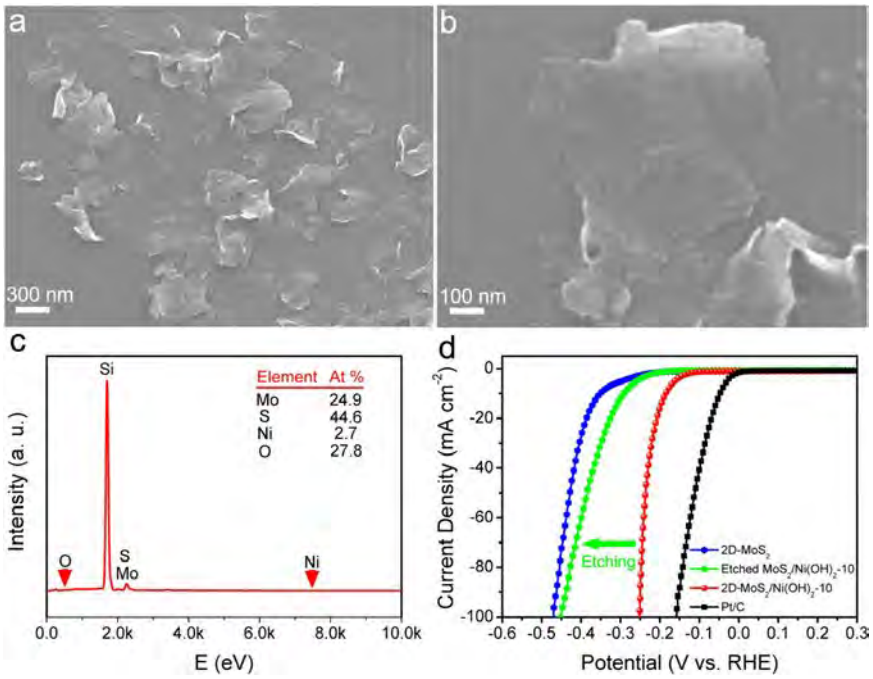

Figure S17. (**a**,**b**) SEM images of etched MoS_2/$Ni(OH)_2$-10 and corresponding (**c**) SEM-EDS in (**b**). (**d**) HER activity of etched MoS_2/$Ni(OH)_2$-10, 2D-MoS_2/$Ni(OH)_2$-10, 2D-MoS_2 and Pt/C in 1 M KOH.

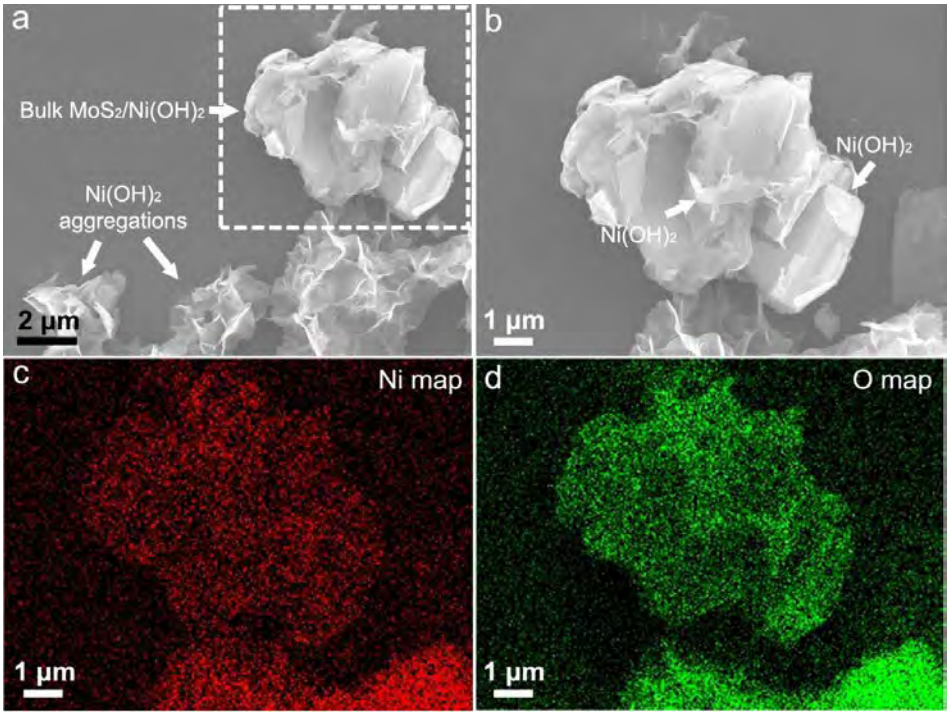

Figure S18. (**a,b**) SEM images of bulk $MoS_2/Ni(OH)_2$ hybrid, and (**b**) shows SEM image of enlarged area (while square) in (**a**) and its corresponding (**c**) Ni EDS mapping and (**d**) O EDS mapping.

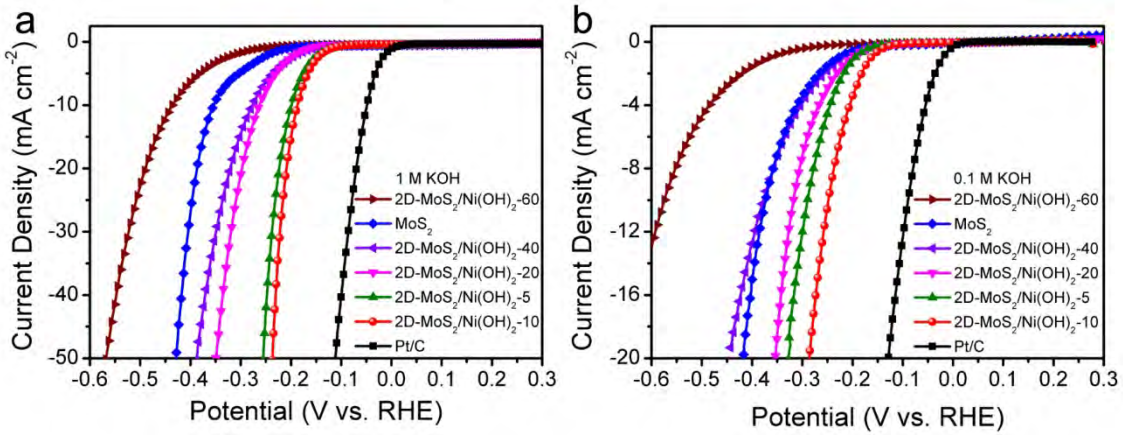

Figure S19. HER activity of 2D-MoS_2/$Ni(OH)_2$-n hybrids with different ratio of $Ni(OH)_2$ to MoS_2 in (**a**) 1 M KOH and (**b**) 0.1 M KOH.

The controllable growth of $Ni(OH)_2$ on the MoS_2 monolayer provides us the opportunity to optimize the HER activity. Figure S19a,b compare HER performances of MoS_2/$Ni(OH)_2$-n (n = 5, 10, 20, 40 and 60), 2D-MoS_2 and Pt/C. It is clear that 2D-MoS_2/$Ni(OH)_2$-10 displays the best performances in 1 M and 0.1 M KOH.

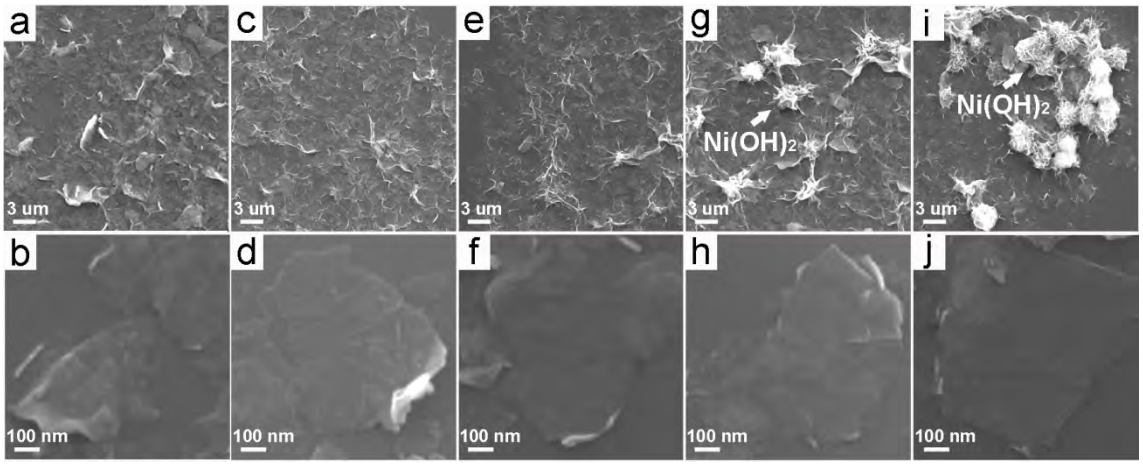

Figure S20. SEM images of 2D-MoS_2/$Ni(OH)_2$-n hybrids with different ratio of $Ni(OH)_2$ to MoS_2: (**a**,**b**) 2D-MoS_2/$Ni(OH)_2$-5, (**c**,**d**) 2D-MoS_2/$Ni(OH)_2$-10, (**e**,**f**) 2D-MoS_2/$Ni(OH)_2$-20, (**g**,**h**) 2D-MoS_2/$Ni(OH)_2$-40, (**i**,**j**) 2D-MoS_2/$Ni(OH)_2$-60.

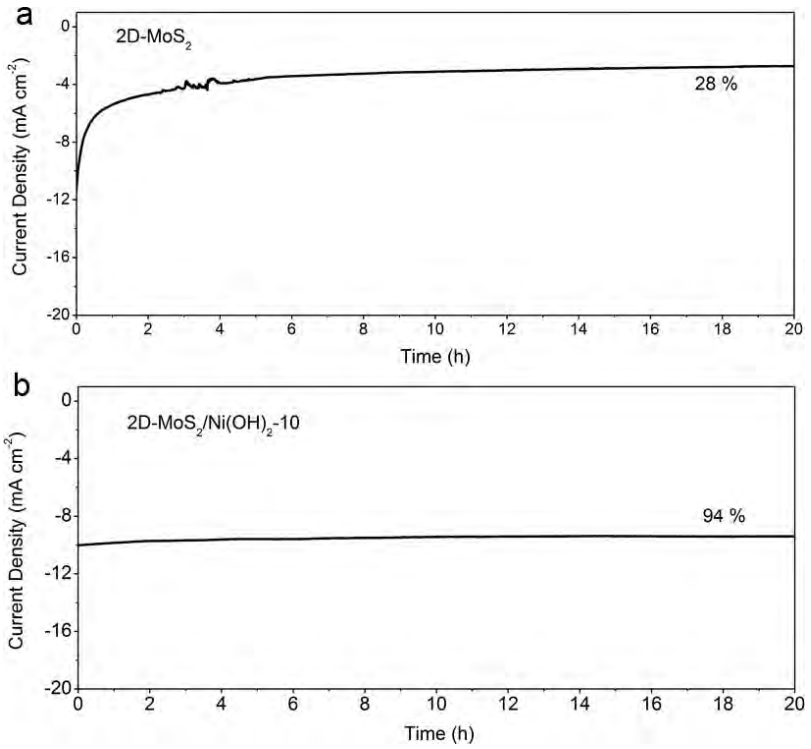

Figure S21. (**a, b**) Chronoamperometric responses of 2D-MoS_2 and 2D-MoS_2/$Ni(OH)_2$-10 in 1 M KOH under the applied potentials of -0.35 V and -0.19 V, respectively.

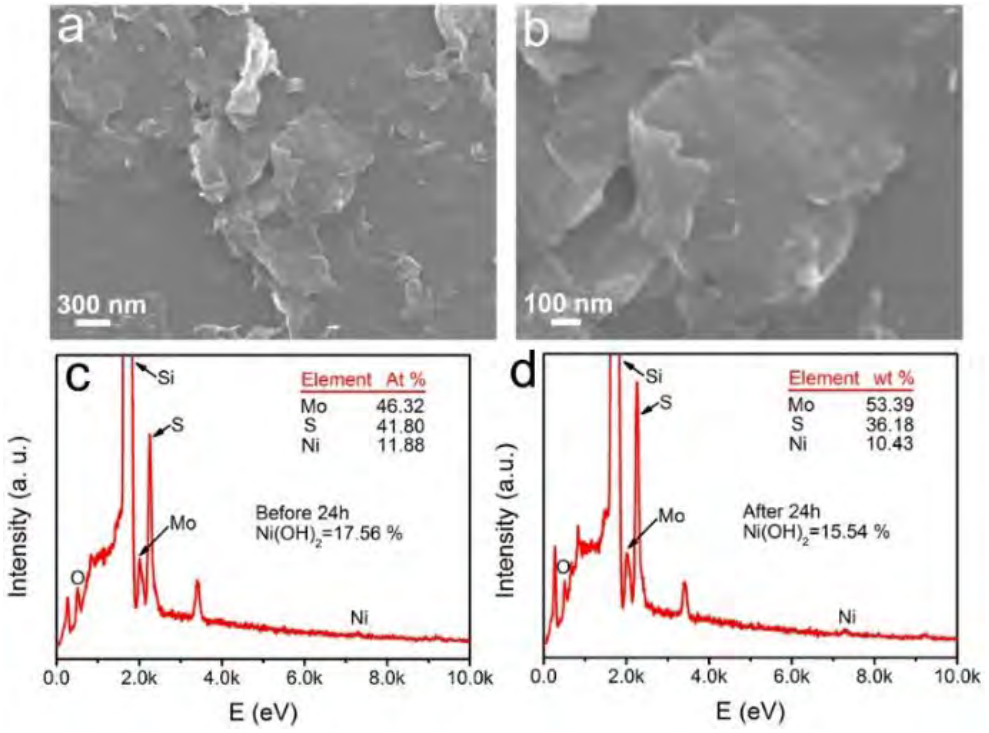

Figure S22. (a, b) SEM images of 2D-MoS_2/$Ni(OH)_2$-10 after CA test for 20 hours, and (c, d) EDS spectra of 2D-MoS_2/$Ni(OH)_2$-10 before and after CA test.

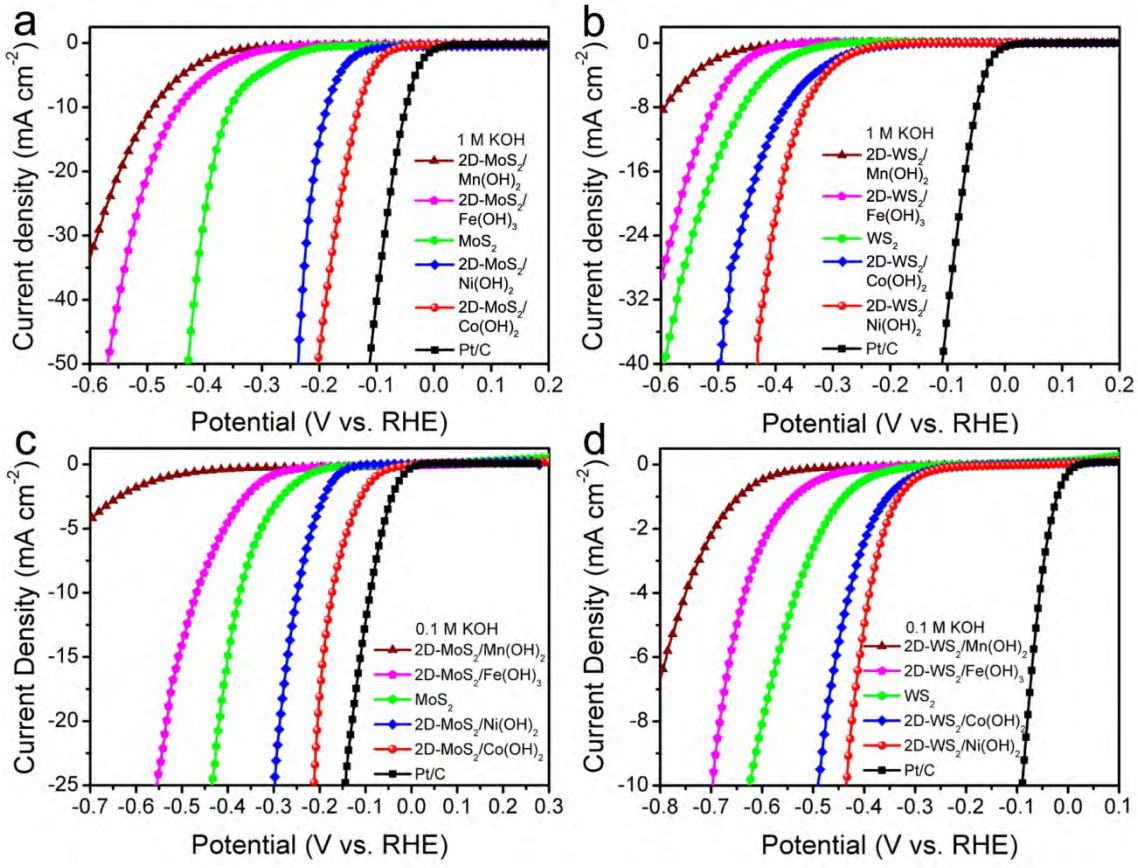

Figure S23. HER activities of 2D-MoS_2-based hybrids modified by 4 kinds of metal hydroxides, bare 2D-MoS_2 and commercial Pt/C (20 wt% Pt) in (**a**) 1 M KOH and (**c**) 0.1 M KOH solution. HER activities of 2D-WS_2-based hybrids modified by 4 kinds of metal hydroxides, bare WS_2 and commercial Pt/C (20 wt% Pt) in (**b**) 1 M KOH and (**d**) 0.1 M KOH solution.

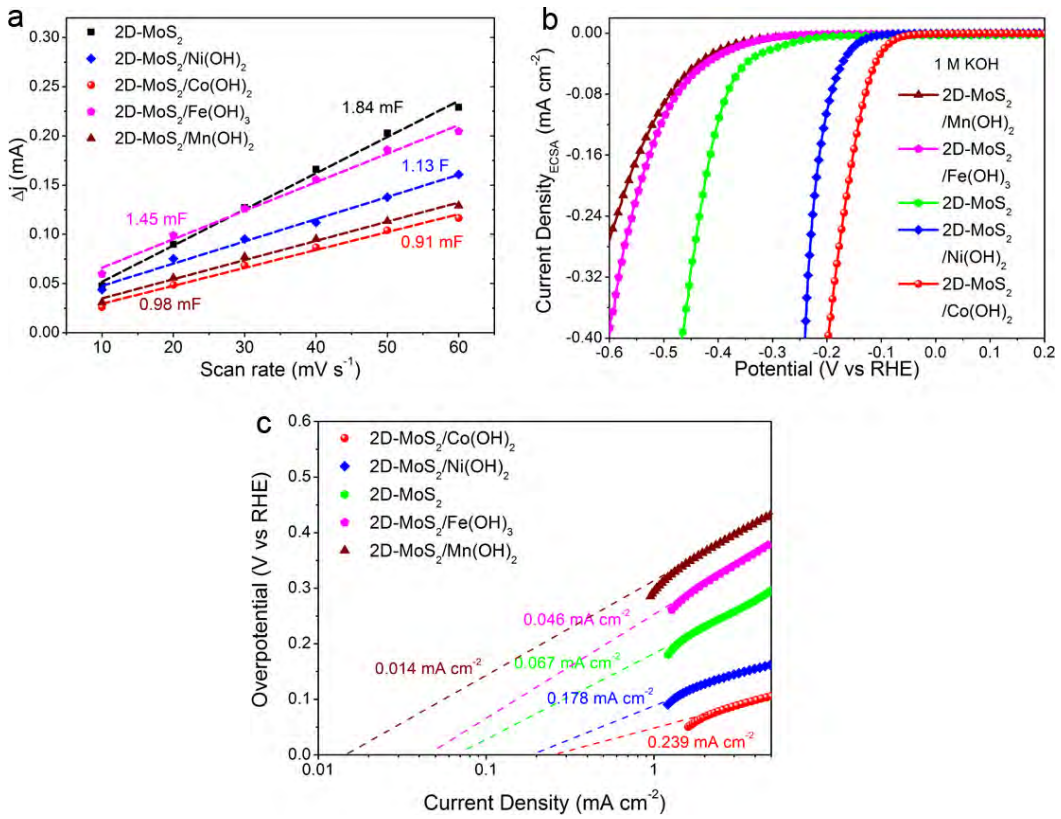

Figure S24. (**a**) The anodic charging currents measured at 0.15 V *vs* RHE plotted as a function of scan rate. (**b**) ECSA-normalized LSV curves and (**c**) The calculated exchange current densities of the 2D-MoS_2, 2D-MoS_2/$Ni(OH)_2$, 2D-MoS_2/$Co(OH)_2$, 2D-MoS_2/$Mn(OH)_2$ and 2D-MoS_2/$Fe(OH)_3$ catalysts via the extrapolation method.

Table S1. Parameters for each electrocatalyst investigated in 1 M KOH

Sample name	C_{DL} (mF)	ESCA (cm^2)	Catalyst ECSA ($m^2\ g^{-1}$)	Exchange Current Density ($mA\ cm^{-2}$)
2D-MoS_2	1.84	46.0	82.3	0.067
2D-MoS_2/$Ni(OH)_2$-10	1.13	28.3	50.5	0.239
2D-MoS_2/$Co(OH)_2$-10	0.91	22.8	40.7	0.178
2D-MoS_2/$Fe(OH)_3$	1.45	36.2	64.9	0.046
2D-MoS_2/$Mn(OH)_2$	0.98	24.4	43.6	0.014

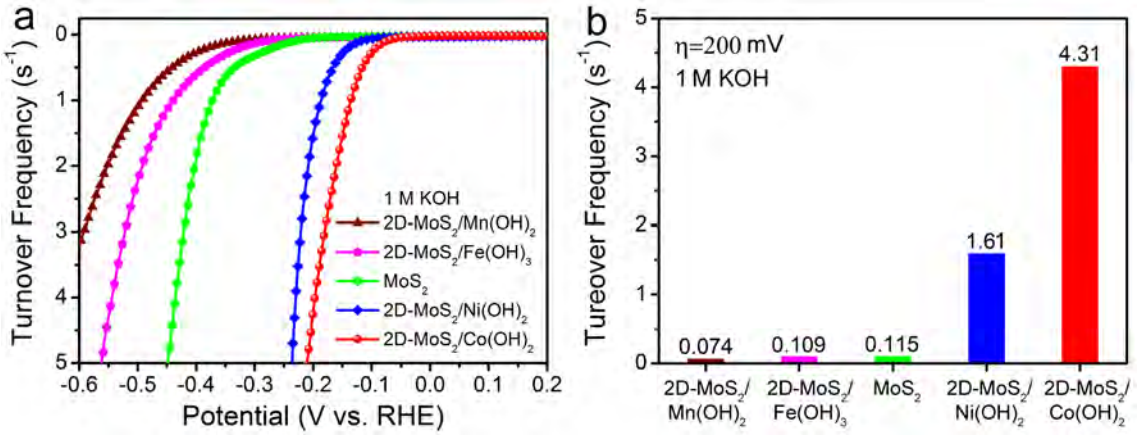

Figure S25. **(a)** The calculated turnover frequencies (TOF_{ac}) values for the different 2D-MoS_2-based electrocatalysts based on measured active sites. The measurement method of active sites was according to work of Hu et al (Chem. Sci., 2011, 2, 1262). **(b)** Corresponding TOF_{ac} values at overpotential of 200 mV.

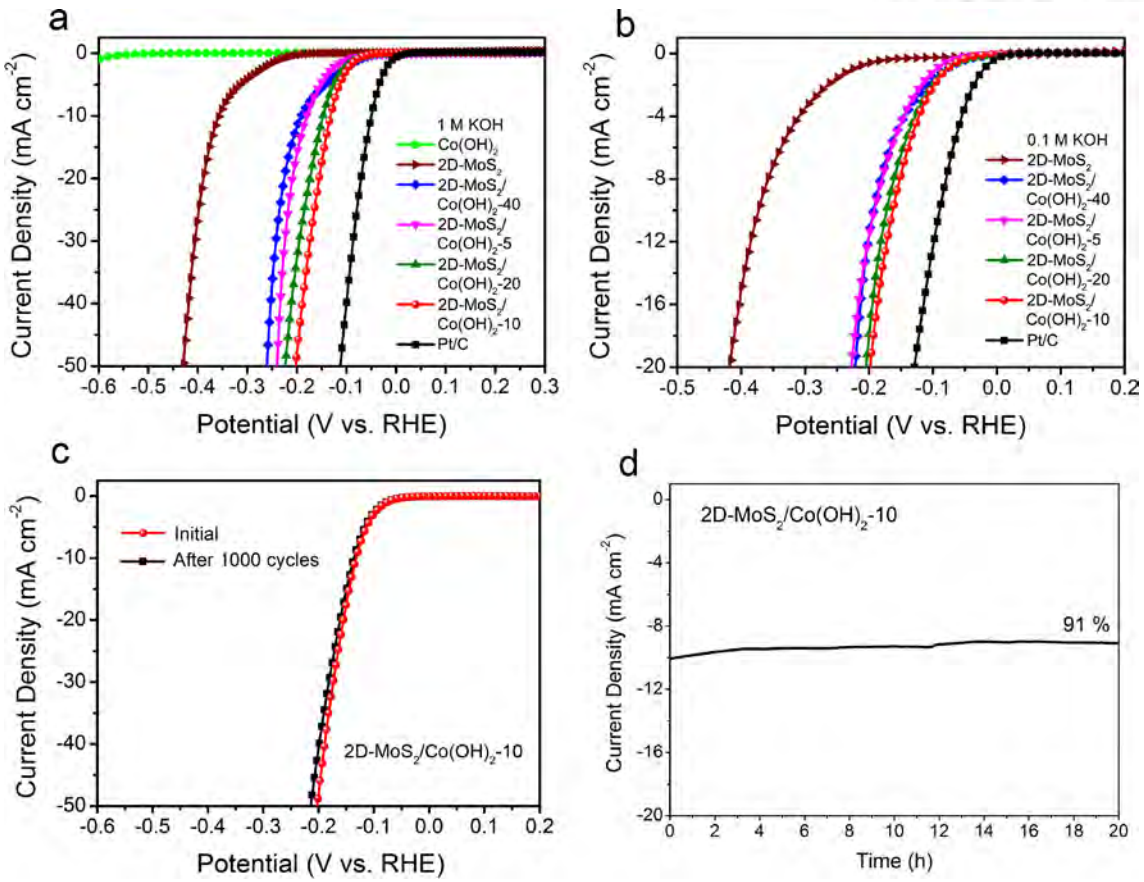

Figure S26. HER performance of 2D-MoS_2/$Co(OH)_2$-n hybrids in (**a**) 1 M KOH and (**b**) 0.1 M KOH. (**c**) Cycle stabilities of most active 2D-MoS_2/$Co(OH)_2$ (also is 2D-MoS_2/$Co(OH)_2$-10) in 1 M KOH (Scan rate: 100 mV s^{-1}) and (**d**) Chronoamperometric responses of 2D-MoS_2/$Co(OH)_2$-10 in 1 M KOH under the applied potentials of -0.13 V vs RHE.

Table S2. Summary of the HER performances of nonprecious materials based electrocatalysts in alkaline electrolytes published since 2016.

Electrocatalyst	Electrolyte and Electrode	Loading density (mg cm^{-2})	Counter Electrode	Overpotential (mV@10 mA cm^{-2})	Tafel Slope (mV dec^{-1})	Reference
2D-MoS_2/$Co(OH)_2$	1 M KOH; Glassy Carbon	0.285	Graphite Rod	125	76	This work
2D-MoS_2/$Ni(OH)_2$	1 M KOH; Glassy Carbon	0.285	Graphite Rod	185	73	This work
Amorphous $CoMoS_x$ Gel	0.1 M KOH; Glassy Carbon	0.176	Graphite Wire	210 @ 5 mA cm^{-2}	-	*Nat. Mater.* **2016**, *15*, 197-203
Hollow Chevrel-Phase $NiMo_3S_4$	0.1 M KOH; Glassy Carbon	0.3	Graphite Rod	275	98	*Angew. Chem. Int. Ed.* **2016**, *55*, 15240-15245
c-$CoSe_2$	1 M KOH; Glassy Carbon	~ 0.1	Graphite Rod	~ 320	-	*Adv. Mater.* **2016**, *28*, 7527-7532
MoB/*g*-C_3N_4 Interface Material	1 M KOH; Glassy Carbon	0.25	Graphite Rod	133	46	*Angew. Chem. Int. Ed.* **2018**, *57*, 496-500
NiS_2 hollow microspheres	1 M KOH; Glassy Carbon	0.21	Graphite Rod	219	157	*J. Mater. Chem. A* **2017**, *5*, 20985-20992
MoP@C	1 M KOH; Glassy Carbon	0.354	Graphite Rod	81	55.6	*Energy Environ. Sci.*, **2017**, *10*, 788-798
N-Mo_2C NSs	1 M KOH; Glassy Carbon	0.357	Carbon Rod	140	66	*ACS Nano* **2017**, *11*, 12509-12518
Mo-SAs@N-Carbon	1 M KOH; Glassy Carbon	0.408	Graphite Rod	132	90	*Angew. Chem.* **2017**, *129*, 16302-16306.
1T $MoS_2/Ni^{2+\delta}O_\delta(OH)_{2-\delta}$	1 M KOH; Glassy Carbon	0.500	Graphite Rod	185	77	*Adv. Sci.* **2018**, *5*, 1700644

Mo_2C-C	1 M KOH; Glassy Carbon	0.84	Graphite Rod	133	82	*Nano Energy* **2017**, *32*, 511-519
Mo_2C/OMC-3	1 M KOH; Glassy Carbon	-	Carbon Rod	175	64	*ACS Appl. Energy Mater.* **2018**, *1*, 736-743
Cu NDs/Ni_3S_2 NTs-CFs	1 M KOH; Carbon Fibers	0.52	Graphite Rod	128	76.2	*J. Am. Chem. Soc.* **2018**, 140, 610-617
Ni-MoS_2-CC	1 M KOH; Carbon Cloth	0.89	Graphite Rod	98	60	*Energy Environ. Sci*. **2016**, *9*, 2789-2793
Ni-Co-MoS_2 Nanoboxes	1 M KOH; Glassy Carbon	0.285	Pt Disc	155	51	*Adv. Mater.* **2016**, *28*, 9006-9011
MoP/SNG-20	1 M KOH; Glassy Carbon	0.5	Pt Wire	49	31	*ACS Catal.* **2017**, *7*, 3030-3038
Mo_2C@2D-NPC	1 M KOH; Glassy Carbon	0.738	Pt Wire	45	46	*ACS Nano* **2017**, *11*, 3933-3942
$Ni_{0.89}Co_{0.11}Se_2$ MNSN/NF	1 M KOH; Nickel Foam	2.2	Pt Plate	85	42	*Adv. Mater.* **2017**, 1606521
$Ni(OH)_2$/MoS_2 Heterostructure	1 M KOH; Carbon Cloth	4.8	Pt Foil	80	60	*Nano Energy* **2017**, *37*, 74-80
CoMnCH@NF	1 M KOH Nickel Foam	5.6	Pt Wire	180	-	*J. Am. Chem. Soc.* **2017**, *139*, 8320-8328